Energy & Environmental Science

ROYAL SOCIETY OF CHEMISTRY

REVIEW

View Article Online
View Journal

Cite this: DOI: 10.1039/d2ee01037b

Single atoms meet metal–organic frameworks: collaborative efforts for efficient photocatalysis

Hongda Liu,[a] Min Cheng,*[a] Yang Liu,*[b] Jun Wang,[b] Gaoxia Zhang,[a] Ling Li,[a] Li Du,[a] Guangfu Wang,[a] Suzhao Yang[a] and Xinya Wang[a]

Received 30th March 2022,
Accepted 12th July 2022

DOI: 10.1039/d2ee01037b

rsc.li/ees

Photocatalysts with metal single atoms (SAs) as active sites have attracted widespread interest owing to their maximum atomic utilization efficiency, well-defined active centers and outstanding photocatalytic activity. In recent years, metal–organic frameworks (MOFs) have emerged as promising supports/precursors to create single atom catalysts (SACs) because of their high porosity, functional adjustability, structural tailorability, and abundant potential anchoring sites. This review aims to provide a comprehensive summary of the development of MOF-supported SACs for efficient photocatalysis. Firstly, the roles of MOFs and SAs in photocatalytic systems and their synergistic effects in boosting photocatalytic performance are thoroughly discussed. Subsequently, the types of SAs supported on MOFs are categorized to reveal their formation process and coordination environment. Furthermore, the advanced characterization tools for identifying and examining the atomic structure of SAs supported on MOFs are highlighted. Thereafter, the advances of MOF-supported SACs for photocatalytic energy conversion are also comprehensively introduced, including the CO_2 reduction and hydrogen generation reaction. Finally, insights into the technical challenges are provided and the future research directions are proposed, which will hopefully stimulate the design of advanced MOF-supported SACs for efficient photocatalysis.

Broader context

Single atom catalysts (SACs) with well-defined active sites and maximum atom utilization efficiency, because of their charming strengths in enhancing light harvesting, charge transfer kinetics, and surface reactions, have fueled the exploration of photocatalysis. Metal-organic frameworks (MOFs) have emerged as promising materials to support single atoms (SAs) for efficient photocatalysis owing to their superior properties of highly crystalline structures, tailored functionality, excellent tailorability, ultrahigh surface areas, abundant potential coordination sites, as well as semiconductor-like behavior. Consequently, a comprehensive and timely review on the dazzling advantages of MOF-supported SACs in photocatalysis is of great importance for the diversity of the development of SACs in photocatalysis. Herein, this review begins by describing the potential roles of MOFs and SAs in photocatalytic systems. The anchoring and coordination mechanisms of SAs supported on MOFs are then briefly discussed. Thereafter, the current available characterization techniques for MOF-supported SACs are assessed. Moreover, the photocatalytic applications and future perspectives for MOF-supported SACs are also highlighted. We anticipate that this review will provide valuable insights for the future discovery of MOF-supported SACs, significantly contributing to the development of efficient photocatalysts for better utilization of solar energy.

1. Introduction

With environmental pollution and energy crisis rising, a green and sustainable source of energy and chemicals is essential to meet the energy demand of modern lifestyles.[1] One of the most effective strategies to address this scientific challenge is to develop a technologically promising chemical process which ensures the supply of renewable and clean energy, thereby reducing the harmful environmental pollution related to the consumption of fossil fuels. Solar energy has been considered as one of the most attractive alternative energy sources due to its abundance, cleanliness, security and sustainability.[2,3] Meanwhile, achieving efficient solar-to-chemical energy conversion by photocatalysis has drawn increasing attention to the production of renewable and clean energy.[4,5]

In general, the performance of photocatalysts is closely correlated with the amount of exposed active sites. Theoretical and experimental studies have confirmed that the strategy of reducing the metal size of catalysts from particles to

[a] College of Environmental Science and Engineering, Key Laboratory of Environmental Biology and Pollution Control (Ministry of Education), Hunan University, Changsha 410082, China. E-mail: chengmin@hnu.edu.cn
[b] School of Minerals Processing and Bioengineering, Key Laboratory of Biohydrometallurgy of Ministry of Education, Central South University, Changsha 410083, China. E-mail: liuyang_feiyang@163.com

nanoparticles (NPs), clusters or even single atoms (SAs) can be effective in increasing catalytic activity and reducing costs.[6–11] In extreme cases, metal SAs are fully exposed as photocatalytic centers to maximize the atomic efficiency, which offers a desirable strategy to produce highly efficient photocatalysts.[12–15] In 2011, Zhang *et al.* successfully supported Pt SAs on iron oxides for highly active and stable CO oxidation by a co-precipitation method for the first time, and proposed the concept of single atom catalysts (SACs), where isolated SAs as well-defined active centers were dispersed on a suitable support without any kind of interaction between each individual atom.[14] Since then, SAs, the ultimate size confinement for metal NPs, with nearly identical microenvironments, quantum size effects and relatively uniformly well-defined active sites, have attracted a great deal of attention in the field of catalysis and are emerging as a vigorous research frontier.[16–19] Advantageously, well-defined SAs in photocatalytic systems will not only multiply the active sites for photocatalytic reactions, but also increase the range of light-harvesting and boost the efficiency of charge separation/transfer.[20,21] However, isolated SAs may easily aggregate into NPs during the reaction because of their high surface free energy.[22,23]

An ideal support is thus needed to provide abundant anchor sites to stabilize the SAs, then realizing the controlled synthesis of SACs.[24,25] Moreover, the supports may also interact with SAs and alter their coordination environment, which could further modulate the activity, selectivity and stability of SAs.[26–28] Therefore, the underlying supports play a decisive role in influencing the structure–performance relationship.[29] It has been established in previous studies that surface defects on metal oxide supports outperform in transforming the electronic structure to match SAs.[30–33] However, these bulk particles suffer from a lack of pore space and inhibit atomic migration, which is critical for fast kinetics of the reaction.[12] The carbon-based supports, such as carbon nanotubes and graphene, can tightly bind with SAs due to the presence of heteroatoms (N, P, O, and S) and defects, and they demonstrate attractive activity, selectivity and durability in the field of catalysis.[20,34–36] Recently, metal–organic frameworks (MOFs), a class of porous and hybrid crystalline structures consisting of metal clusters and organic linkers, are considered as ideal platforms for stabilizing SAs.[37–41] MOFs have been successfully shown to support and stabilize metal NPs well together with the synergistic catalytic effect.[42,43] Similarly, MOFs can also provide abundant potential coordination sites to anchor SAs and prevent them from aggregating.[44] SAs can be easily introduced into the metal oxo clusters with coordinatively unsaturated metal sites, the organic linkers with adjacent available coordination atoms of MOFs.[45,46] Interestingly, MOFs present great flexibility in physicochemical properties (chemical, thermal and mechanical stability) owing to their tunable chemical composition and tailorable structure caused by fine control of the inorganic and organic components.[47] Moreover, MOFs can provide diverse functional anchoring sites to modulate the coordination microenvironment of SAs *via* pre-synthetic and post-synthetic modification.[48,49] These may endow them with a wide range of versatility to be efficiently employed under various photocatalytic conditions. Furthermore, the high-specific-area and large surface area of MOFs can offer high-throughput reaction interfaces to facilitate the diffusion of reactants to the well-defined active sites.[50,51] More importantly, the linkers in MOFs are capable of capturing photons, thus inducing charge separation, which confirms their feasibility and advantage as photosensitive units in photocatalysis.[52,53] Therefore, MOFs can be ideal supports for the intercalation of SAs to achieve high-performance photocatalysis.

Current research related to SACs is well advanced and there are some outstanding reviews with an emphasis on the background of SACs and their applications. Zheng *et al.* have systematically discussed non-carbon-supported SACs for electrochemical energy conversion.[54] Recently, Xue *et al.* comprehensively reviewed the SACs for photocatalytic energy conversion.[55] To the best of our knowledge, some excellent reviews have appeared in the literature highlighting the background and synthetic strategies of MOF-supported SACs, as well as their great advantages for electrocatalysis.[56–58] In addition, research on the application of MOF-supported SACs in photocatalysis is still in its infancy, and the primary working mechanisms of SAs and MOFs which are closely related to light-harvesting and charge separation/transfer are ambiguous. Hence, for the purpose of promoting this new and rapidly developing field, a timely review of recent exciting developments of MOF-supported SACs in photocatalysis is highly desirable, which will contribute to the rational design and preparation of more efficient MOF-supported SAC photocatalysts and inspire future research directions. In this review, we dedicatedly begin with a thorough introduction to the superior efficacy of SACs in photocatalysis attributed to their ability to tune light-harvesting, charge transfer kinetics, and surface reactions to gain a comprehensive understanding of the structure–performance relationship of SACs in photocatalysis. Second, the types of MOF-supported SACs will be concisely discussed to reveal their formation process and coordination environment. Thirdly, the advanced characterization techniques for the detection of MOF-supported SAC photocatalysts are systematically summarized. Fourth, their corresponding photocatalytic applications have been thoroughly covered on the basis of photocatalytic reactions, such as hydrogen generation and CO_2 reduction. Finally, a concise conclusion is presented and the perspectives and challenges of MOF-supported SACs for photocatalytic applications are discussed. We anticipate that this review will shed new light on this subject and stimulate the understanding and discovery of MOF-supported SACs, contributing to the expeditious development of this emerging field of research.

2. Principles of MOF-supported SACs in photocatalysis

2.1. Photocatalytic processes

It is well known that light-harvesting units and photocatalytically active sites are the two key components in a photocatalytic system. For MOF-supported SAC photocatalysts, the MOFs and

SAs normally act as light-harvesting units and photocatalytically active sites, respectively. The potential of MOF-supported SACs for photocatalytic processes arises from their redox ability under exposed light conditions. Specifically, the photoreaction process consists of three main steps as follows (Fig. 1): (a) absorption of photons by the MOF-supported SACs to produce electron–hole pairs and the separation of excited charge carriers (electrons and holes) within the MOF-supported SACs;[59] (b) transport of electrons and holes to the surface of MOF-supported SACs;[60] and (c) redox reactions (hydrogen generation, CO_2 photoreduction and so on) of the charges on the surface of MOF-supported SACs.[61] The overall efficiency of the photoreaction process is determined by the kinetics and thermodynamics related to each of these steps (light-harvesting, charge separation and transfer, and surface redox photoreaction). In the first step of the photoreaction process, the band gap width and morphology of the MOF-supported SACs largely influence the separation efficiency of electron–hole pairs. During the second step of the photoreaction, oppositely charged electrons and holes may recombine during transport due to the mutual attraction at surface sites and dissipate energy as heat or light energy.[62–64] The interactions between the two components (MOFs and SAs) are tightly correlated with the charge transfer kinetics, which largely determines the whole performance of the MOF-supported SAC photocatalytic system. Third, photocatalysis requires a great number of photocatalytically active sites to provide a suitable environment for charge separation or reagent adsorption, thereby facilitating the photocatalytic reactions on the surface of MOF-supported SACs with extreme efficiency. Notably, the role of the SAs in the photocatalytic system transcends beyond that of the photocatalytic active sites. Similarly, MOFs as supports are by no means limited to their role as the light-harvesting units. The next step will thoroughly elucidate the potential and overall roles of these two components (MOFs and SAs) in determining the whole performance of the photocatalytic system.

2.2. Bright sparks of MOFs and SAs in photocatalysis

Significantly different from their bulky counterparts, SACs are composed of isolated metal SAs immobilized on supports or individual metal core complexes, which provide maximum atomic efficiency and metal active sites, making them one of the most desirable approaches to creating efficient photocatalysts.[65,66] MOFs are a class of crystalline porous materials with well-defined and tailorable structures, high surface area and abundant potential chelation sites, which have been regarded as ideal supports for strongly and firmly stabilizing SAs with superior atomic dispersion and high metal loading. In photocatalytic systems with MOF-supported SACs as photocatalysts, the SAs normally act as the photocatalytically active sites to enhance the activity and selectivity of the photocatalytic reaction. Moreover, the decoration of metal SAs with the unique electronic structures in MOFs could be employed to modulate the band structure to increase the light-harvesting capability of semiconducting-like MOF supports. In the following part, the dramatic roles of MOFs in the construction of SACs with high metal loading and excellent stability but without aggregation will be thoroughly elucidated. In addition, the potential roles of atomically dispersed SAs in influencing light-harvesting, charge transfer kinetics, and surface photoreaction will be comprehensively discussed.

On the one hand, MOFs play the following key roles in improving the atomic dispersion, loading and stability of SAs (Fig. 2a).

(1) The enormous surface energy of SAs inevitably leads to their aggregation into metal nanoclusters and even large-scale metal NPs, especially under extreme reaction conditions.[67]

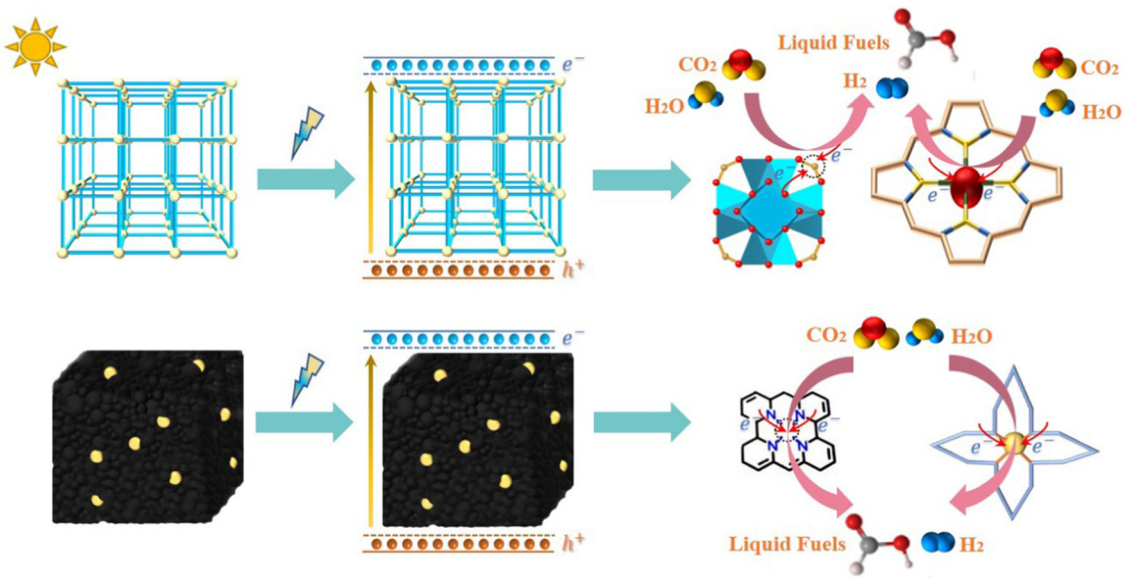

Fig. 1 Schematic illustration of the main processes for the MOF-supported SACs in photocatalysis.

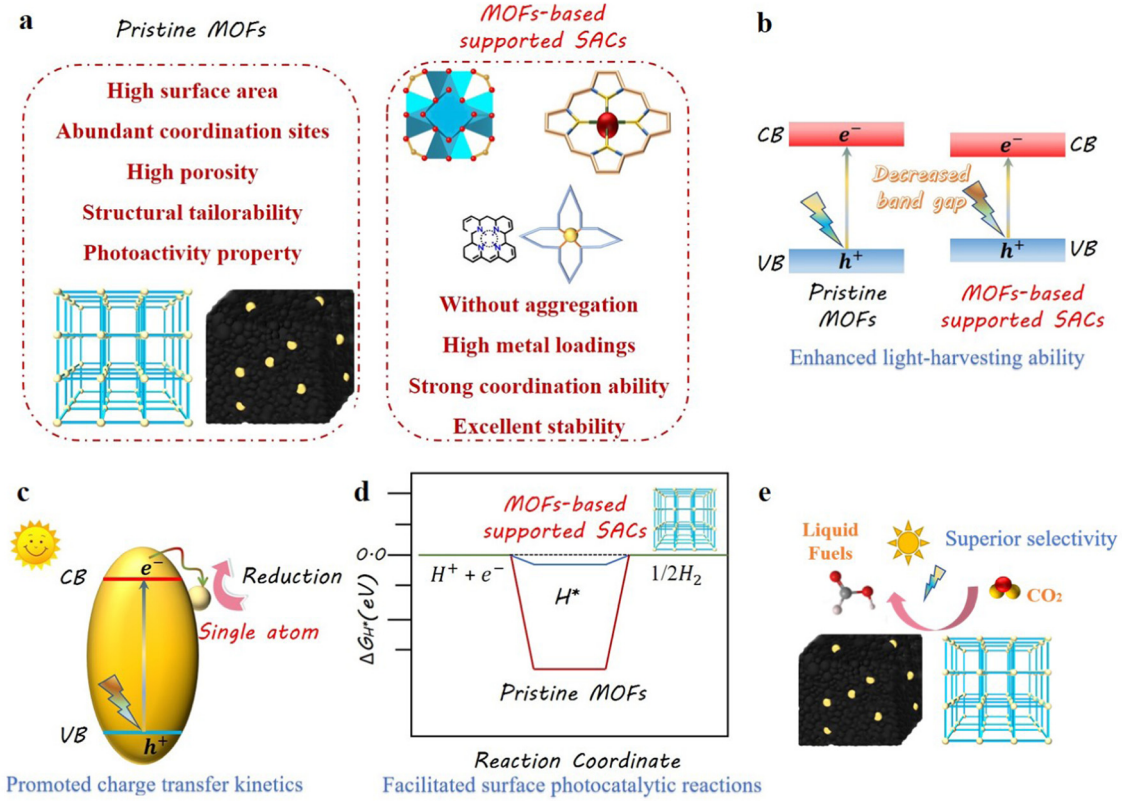

Fig. 2 (a) Schematic illustration of the potential advantages of MOFs for the construction of SACs in photocatalysis. Schematic illustration of (b) enhanced light-harvesting ability, (c) promoted charge transfer kinetics, (d) facilitated surface photocatalytic reactions and (e) superior selectivity of the MOF supported SAC photocatalyst compared to the pristine MOFs.

MOFs, consisting of secondary building units and linkers, exhibit a long-range ordered structure with alternating arrangements of inorganic clusters and organic linkers, which can act as ideal supports to stabilize SAs within the frameworks prior to and during MOF synthesis. In sharp contrast to traditional inorganic supports that stabilize SAs only at their surface, the organic linkers and inorganic clusters within MOFs can provide various anchoring sites for the immobilization of additional metal SAs and keep them from aggregating. In the case of the organic linkers, donor sites in suitable organic linkers of MOFs such as N, O, *etc.*, will supply abundant potential coordination sites ready to stabilize SAs.[59,68] In anchoring SAs into inorganic clusters, mainly Zr_6 clusters, some designedly defective MOFs can offer exposed coordinatively unsaturated metal sites to anchor SAs into the host frameworks, such as the –OH/OH_2 groups on the Zr_6 clusters.[69,70] Based on these strategies, SACs can be well anchored within the host frameworks, which will greatly preserve the high dispersion of SAs and prevent their aggregation during photocatalytic reaction, resulting in efficient photocatalysis.

(2) Photocatalytic activity increases with the proportion of SAs. Recent reports demonstrate that the high-metal-loading and thermally stable SACs have achieved unprecedented catalytic performance.[71,72] For example, Xiong *et al.* reported that isolated Fe atoms can be stabilized through a pyrolyzing coordinated polymer strategy, yielding SACs with a record metal loading of 30 wt% at the gram scale, which exhibited excellent catalytic activity in the epoxidation of styrene and met the requirements of industrial catalysis.[72] However, most reported SACs always exhibit relatively low metal content and are difficult to control and reproduce, which are major obstacles to fulfill the demand of practical applications.[73–76] Thus, it is of importance to develop novel and general strategies to construct SACs with high metal loading and prevent their aggregation into other undesired species. Interestingly, MOFs can provide abundant available chelating sites to stabilize more SAs for more efficient photocatalytic activity without aggregation. Zuo *et al.* recently employed a surfactant-stabilized coordination strategy to construct ultrathin MOF nanosheets supporting Pt SAs for photocatalytic hydrogen generation.[77] The ultrathin MOF nanosheets were constructed from $Cu_2(COO)_4$ paddle-wheel clusters and Pt(II) tetrakis(4-carboxyphenyl)porphyrin (PtTCPP) as the organic linkers. The porphyrin rings from organic linkers played a critical role in anchoring the Pt SAs. The Pt atoms could be coordinated with the porphyrin rings before MOF formation, thus avoiding Pt aggregation and hence formation of other undesired species and allowing a relatively high loading of 12 wt% Pt SAs on MOFs. Moreover, the MOFs can be universally extended to stabilize many other types of SAs, which breaks the limits of an identical chemical microenvironment. He *et al.*

reported a facile solvothermal strategy to prepare zirconium–porphyrinic MOF hollow nanotubes to support a series of SAs (Ir, Ru, Pt, Au and Pd) for visible-light photocatalytic hydrogen generation.[59] Specifically, a series of SAs supported on MOFs were prepared by treating with the corresponding metal salts, as-synthesized MOFs and DMF at 80 °C for 4 h. More importantly, the addition of a suitable mediator during the preparation of MOF-supported SACs could not only allow the introduction of different SAs, but could also change the MOF supports, thus achieving the synthetic universality. Sui *et al.* have consolidated the strengths of MOFs as supports and SnO_2 as mediators or adaptors, and developed a general synthetic protocol to anchor diverse SACs (Cu, Pt and Ni) onto SnO_2 furnished different MOFs (PCN-222, UiO-66-NH_2 and DUT-67).[78] The MOFs were first impregnated with Sn^{2+} and then the metal precursors were introduced under microwave-assisted conditions. Subsequently, the sufficiently dispersed Sn^{2+} could undergo redox and hydrolysis reactions with the introduced metal precursors, resulting in the deposition of metal SAs onto the SnO_2 captured in the MOFs. Such a synthetic route breaks through the restrictions for specific SAs and MOFs and greatly improves the generality of the synthesis.

(3) The confinement of SAs in the MOFs not only allows for high metal loading but, more importantly, also ensures excellent stability of the SAs. In general, the stability and reusability are important factors for the applicability of a photocatalyst. The weak affinity between conventional supports and SAs can limit the reusability of SACs as photocatalysts, thus seriously limiting the achievement of the ultimate photocatalytic efficiency of SACs.[79–81] The MOFs have abundant potential coordination sites in metal oxo clusters and organic linkers to tightly anchor SAs with strong affinity and can be ideal supports to stabilize SAs for photocatalysis. The strong affinity between SAs and MOFs will directly determine their durability. Also, the MOF support needs to be able to withstand the conditions appropriate for the targeted reaction. Interestingly, due to good designability and excellent tailorability, MOF supports have graduated from the realm of 'usually moisture sensitive' and 'usually delicate' to virtually conventional designable to tolerate harsh physical and chemical conditions.[47] For example, due to the highly oxygenophilic capability of Zr^{4+} and 12-coordinated Zr_6 clusters, UiO-66 is stable in water and resists well moderately acidic or alkaline solutions and has been extensively used as a support for stabilizing SAs.[69,82] MIL compounds, another example of widely studied MOFs in this area, which are comprised of carboxylate-terminated linkers and trimeric metal clusters (including Al, Cr and Fe), also demonstrate good stability in water.[83–85] In addition, some of the newly developed MOFs, such as the aluminum-based porphyrinic MOF, can also show desirable chemical stability.[86] Fang *et al.* reported Pt SAs confined into this aluminum-based porphyrinic MOF for hydrogen generation under visiblelight irradiation.[68] It showed excellent hydrogen generation performance and demonstrated no apparent rate change over the four photocatalytic runs. X-ray diffraction of the powder after the photocatalytic runs revealed the structural integrity and well-maintained crystallinity of the SACs, indicating their high stability under photocatalytic conditions. Moreover, no particles were observed in the structural characterization after the reaction, indicating that Pt remained in its isolated single atomic form and did not aggregate, further confirming the stability of Pt SAs. Similarly, the related works have shown that most of the studied MOF-supported SACs have negligible changes in the crystalline structure and remain in the form of isolated SAs before and after recycling experiments, suggesting the durability and stability of these materials, which derive from the strong affinity between the SAs and MOFs during the photocatalytic reaction.[87,88] In summary, in contrast to other SACs, most of the MOF-supported SACs studied show remarkable stability and reusability during the photocatalytic process, indicating that MOFs are highly attractive supports to anchor SAs.

On the other hand, the introduction of SAs on MOFs may affect their light-harvesting capability, charge transfer kinetics, surface reactions as well as selectivity during the photocatalytic process.

(1) Light-harvesting, the first step in the photocatalytic process, can lead to the generation of electron–hole pairs to carry out the subsequent photocatalytic reactions by absorbing incident photons.[89] The energy band structure of a semiconductor, including the band gap and the conduction band (CB) and valence band (VB) positions, determines its light-harvesting capability.[55] It is important that a narrow band gap of the photocatalyst is typically required to fully utilize solar energy for the generation of photogenerated charge carriers. Moreover, the CB and VB positions of the photocatalyst should match the redox potentials of the targets to initiate the photocatalytic process. It was found that the introduction of SAs could modulate the energy band alignments of MOF supports to enhance the light-harvesting capability (Fig. 2b). For instance, the UV-vis diffuse reflectance (DRS) spectra observed that the coordination of isolated Cu atoms with UiO-66-NH_2 enabled an additional light absorption peak at 500 nm with a tail up to 800 nm.[61] According to density functional theory (DFT) calculations, it was revealed that introduction of Cu SAs into UiO-66-NH_2 shifted both the lowest unoccupied molecular orbital (LUMO) and highest occupied molecular orbital (HOMO) of UiO-66-NH_2 downward, lowering the band gap and thus improving its light-harvesting capability, shifting the Fermi level to the bottom of the LUMO compared to the original UiO-66-NH_2. This was because Cu SAs increased the number of electron migration on the occupied molecular orbitals, which derived from the accelerated electron migration in the occupied molecular orbital.

(2) The introduction of SAs can not only modulate the band gap to improve the light-harvesting capability of MOF supports but can also provide additional transfer channels to accelerate the transfer of photogenerated electrons, hence greatly boosting the surface charge transfer kinetics in the photocatalytic systems of MOF-supported SACs (Fig. 2c). The charge transfer kinetics between the light-harvesting MOF supports and SAs plays a critical role in determining the whole efficiency of the photocatalytic system. Generally, by introducing metals into

the semiconductor, the photogenerated electrons in the semiconductor will be transferred to the loaded metal *via* the Schottky barrier under irradiation.[90] This unique photogenerated charge transfer kinetics in metal–semiconductor can also occur in MOF-supported SAC photocatalysts, which can favorably affect electron transfer and promote electron–hole separation at the interface. SAs within MOFs can act as electron acceptors and active sites for reduction reaction. More strikingly, SAs are the ultimate size of metal NPs, with the unique electronic structures that can beneficially influence the interactions between SAs and light-harvesting MOF supports, and further promote charge transfer kinetics. For instance, Zuo *et al.* revealed that the Pt SAs could minimize the transport distance of the photogenerated charge carriers among the ultrathin 2D MOF nanosheets, hence boosting the photocatalytic hydrogen generation performance.[77] This charge transfer kinetics could be evaluated by the photoelectric experiments. In sharp contrast to pristine MOF nanosheets and Pt NPs on MOF nanosheets, the incorporation of Pt SAs into 2D MOF nanosheets resulted in the highest photocurrent density and the lowest resistance. These results supported that efficient electron transfer channels could be formed between Pt SAs and 2D MOF nanosheets, thus dramatically boosting the charge separation efficiency. This shortened charge transfer between SAs and light-harvesting MOFs could be also observed in other MOF-supported SACs in photocatalysis.[60,78]

(3) SACs can reduce the activation energy or overpotential of photocatalytic reactions, such as water dissociation.[91,92] Studies of hydrogen generation have shown that the active sites with Gibbs free energy values (ΔG_{H^*}) of 0 possess the best hydrogen generation activity. In general, it is difficult for single MOFs to overcome the energy barriers for successful hydrogen generation because the hydrogen intermediates (H* atoms) tend to exhibit unfavorable adsorption on their surfaces, limiting the release of hydrogen.[35] However, the successful incorporation of SAs within MOFs can effectively reduce the reaction activation energy, facilitate the electron–proton process for H* formation, and optimize H-binding to promote hydrogen generation (Fig. 2d). For instance, the incorporation of Pt SAs into the MOFs (Al–TCPP–0.1Pt) can optimize H-binding (ΔG_{H^*} = −0.05 eV) to facilitate hydrogen generation, thus exhibiting excellent photocatalytic hydrogen generation activity.[68] In contrast, Pt NPs enclosed in Al-TCPP and fresh Al-TCPP showed strong hydrogen adsorption for the H*, resulting in unfavorable H* release and thus greatly limiting the activity.

(4) More importantly, as compared with their counterparts, SAs possess unique electronic structures and coordinatively unsaturated sites, which can not only enhance the photocatalytic performance, but can also endow the photocatalytic system with selectivity (Fig. 2e). Wang *et al.* incorporated Cu SAs into UiO-66-NH_2 for photocatalytic CO_2 reduction *via* a photoinduction method.[61] It was found that the introduced Cu SAs facilitated the accumulation of electrons around Cu SAs/UiO-66-NH_2, which accelerated the multielectronic process for photocatalytic CO_2 reduction. The authors further examined a critical intermediate (COOH*) to study the photocatalytic activity as well as the selectivity for CO_2 reduction. The results suggested that Cu sites showed much lower formation energies of CHO* and COOH* than other catalysts. Moreover, Cu SAs/UiO-66-NH_2 featured more suitable free energy changes to produce CO* from *COOH and CHO* from the hydrogenation of *CO compared with Cu and Cu–CuO, facilitating the formation of CO* and CHO* intermediates which could easily undergo coupling on Cu SAs sites to form methanol and ethanol. Consequently, Cu SAs/UiO-66-NH_2 demonstrated excellent selectivity toward the conversion of CO_2 to methanol and ethanol.

3. MOF-supported SACs

With the developments in nanoscience, the reduction in the dimension of metal catalysts to the atomic level has been achieved. SAs, unlike metal NPs or clusters, can offer maximum atomic efficiency, provide tunable electronic structures and enable maximum interactions with reactant molecules, resulting in efficient catalytic performance at a relatively low metal cost.[75] For SACs, the support is an integral part of the system and needs to be painstakingly selected, which should not only provide a number of anchor sites to stably bond the metal with strong interactions, but also create a unique coordination environment to support SAs to ensure activity, selectivity and durability.[54] MOFs are crystalline porous materials with a high degree of order and they consist of metal clusters as well as organic linkers; they have been employed as promising supports to prepare solid and well-positioned dispersed SAs.[93] It is possible to precisely control the dispersion state of SAs by incorporating them into the metal clusters or organic linkers of structurally tailorable MOFs to maintain their stability during the photocatalytic reactions.[94] Up to now, various approaches have been pursued to support and synthesize SACs using MOFs, such as photoreduction, atomic layer deposition, and thermal activation.[61,95,96] In thermally activated preparation strategies, SACs are prepared *in situ* by thermal reduction of appropriate precursors at suitable temperatures under a controlled reducing gas atmosphere, such as N_2, NH_3, Ar or H_2. However, under elevated temperature, the crystal structures of MOFs will be destroyed.[97] SAs can also be strongly anchored on MOF-derived materials through carbonization because of the robust coordinative bonds between heteroatoms (S/O/N) and SAs, leading to the successful preparation of SACs with superior catalytic properties.[98] Herein, recent development of pristine MOF/MOF-derived supports to stabilize well-dispersed SAs is elaborately summarized (Fig. 3).

3.1. Pristine MOF-supported SACs

3.1.1. SAs anchored on metal clusters. Metal clusters in MOFs typically feature coordinately unsaturated metal sites, which can act as available chelating sites to anchor SAs with different structures.[99] For instance, in Zr-MOF, the adjacent –O/OH_x group from the Zr oxo cluster will offer a lone pair of electrons and the charge balance to anchor the additional SAs.[100]

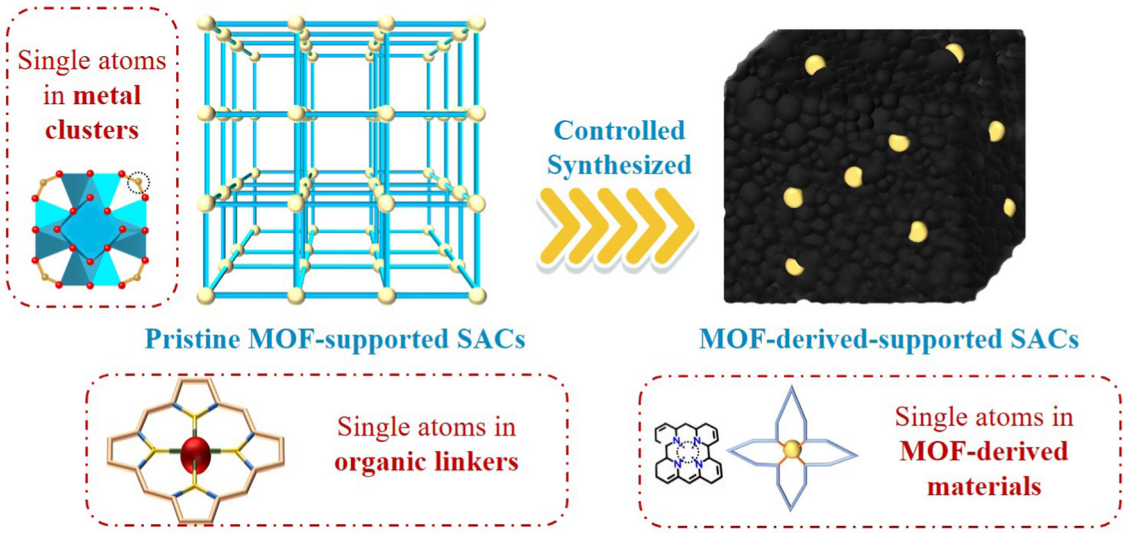

Fig. 3 Schematic illustration of different types of SAs anchored on pristine MOF and MOF-derived supports.

Ma *et al.* reported an innovative approach to prepare Ni-based SACs supported by UiO-66-NH_2 with high-loading (>4 wt%) Ni SAs (Fig. 4a).[70] In their experiment, $NiCl_2{\cdot}6H_2O$ was treated with UiO-66-NH_2 in CH_3CN by a facile microwave-assisted method, and the $-O/OH_x$ groups from the defect sites of the Zr_6 oxo cluster could be effectively coordinated with atomically dispersed Ni^{2+} sites. Moreover, the coordination environment of the Ni_1 site could be further modulated by post-synthetic modification because the coordination between the anchored Ni_1 site and the $-O/OH_x$ group was predominantly present on one side. To achieve this, the authors used thioacetamide and ammonia for hydroxylation and sulphation of Ni^{2+}/UiO-66-NH_2, respectively, which resulted in the generation of Ni_1–O/UiO-66-NH_2 and Ni_1–S/UiO-66-NH_2. Under the air atmosphere, the Ni_1 coordination environment of Ni_1–S/MOF could be further manipulated and partially oxidized to afford Ni_1–S_{ox}/MOF. Apart from this strategy, defects of MOFs can also provide abundant sites for direct anchoring of extraneous metal SAs with isolated dispersion. For instance, in activated UiO-66-NH_2 after defect-engineering, Ir species could be readily anchored onto the Zr oxo clusters through impregnation and annealing treatments to realize Ir_1 SAs/UiO-66-NH_2 particles and membranes with atomically dispersed Ir atoms as the active centers (Fig. 4b).[101] The defective UiO-66-NH_2 was prepared by partially replacing 2-aminoterephthalic acid (the original organic linker of UiO-66-NH_2) with acetates and then removing these acetates at elevated temperatures. In sharp contrast to the pristine UiO-66-NH_2 particles, the defects on defect-engineered UiO-66-NH_2 could offer abundant sites to anchor the extraneous single Ir species to afford SAs/UiO-66-NH_2. Similarly, Abdel-Mageed *et al.*[69] demonstrated that Cu atoms can be covalently attached to the defect sites on the Zr_6 oxo cluster of UiO-66, $Zr_6O_4(OH)_4$-$(C_8H_4O_4)_5$–$(CH_3COO)_{0.7}(H_2O)_{1.3}(OH)_{1.3}$. The defective UiO-66 was prepared by using acetic acid as the modulator with about one missing linker per one Zr_6 cluster, and $-OH/-OH_2$ and acetate groups terminated the defect sites (Fig. 4c). The Cu ions were successfully 3-fold coordinated with two O atoms of $-OH/-OH_2$ groups in UiO-66 and one chlorine atom to afford the Cu/UiO-66 complex by heating UiO-66 with $CuCl_2{\cdot}2H_2O$. After pretreatment with 10% H_2–N_2 at 150 °C, the 3-fold coordinated Cu species were transformed into 2-fold coordinated Cu^+ which combined with two O atoms of the $-OH/-OH_2$ groups on the Zr_6 cluster, thereby forming Cu/UiO-66 with atomically dispersed Cu atoms (Fig. 4d).

In recent studies, the most common approach to creating defects in MOFs is to replace polydentate linkers with monodentate linkers during MOF syntheses, causing deficient occupancy of the linkers at the metal clusters and thereby opening up a large number of coordination sites to anchor the SAs. In addition to the above discussed monodentate linkers, Guo *et al.* reported a low-temperature photoreduction method to synthesize Pt SACs that were enclosed at the defects of Ce-MOFs using formic acid as a modulator (Fig. 4e).[87] The Ce-MOF $(Ce_6O_4(OH)_4)(C_6H_4(COO)^2)_6$ with no defects was the isoreticular topology of UiO-66, and the defects in defective Ce-MOF were created by the addition of formic acid. To prepare SACs, the pre-prepared Pt SAs were preferentially coordinated to the defects in Ce-MOF. The isolated Pt atoms were obtained by freezing an aqueous solution of H_2PtCl_6 in a liquid N_2 bath and then irradiating with ultraviolet light. Because the defect sites in Ce-MOF were atomically dispersed, the Pt atoms could coordinate with these sites in a one-to-one way, enabling the Pt atoms to be uniformly dispersed in the chemically defined environment. These studies emphasize the successful design of pristine MOF-supported SACs with metal SAs anchored on metal clusters.

3.1.2. SAs coordinated with organic linkers. Apart from the metal clusters, the organic linkers provided by MOFs also have strong anchoring properties and can achieve good coordination with SAs. Porphyrins with four pyrrole N sites in the square planar or tetrahedral structure of MOFs have been reported to be effective in trapping metal SAs through coordination

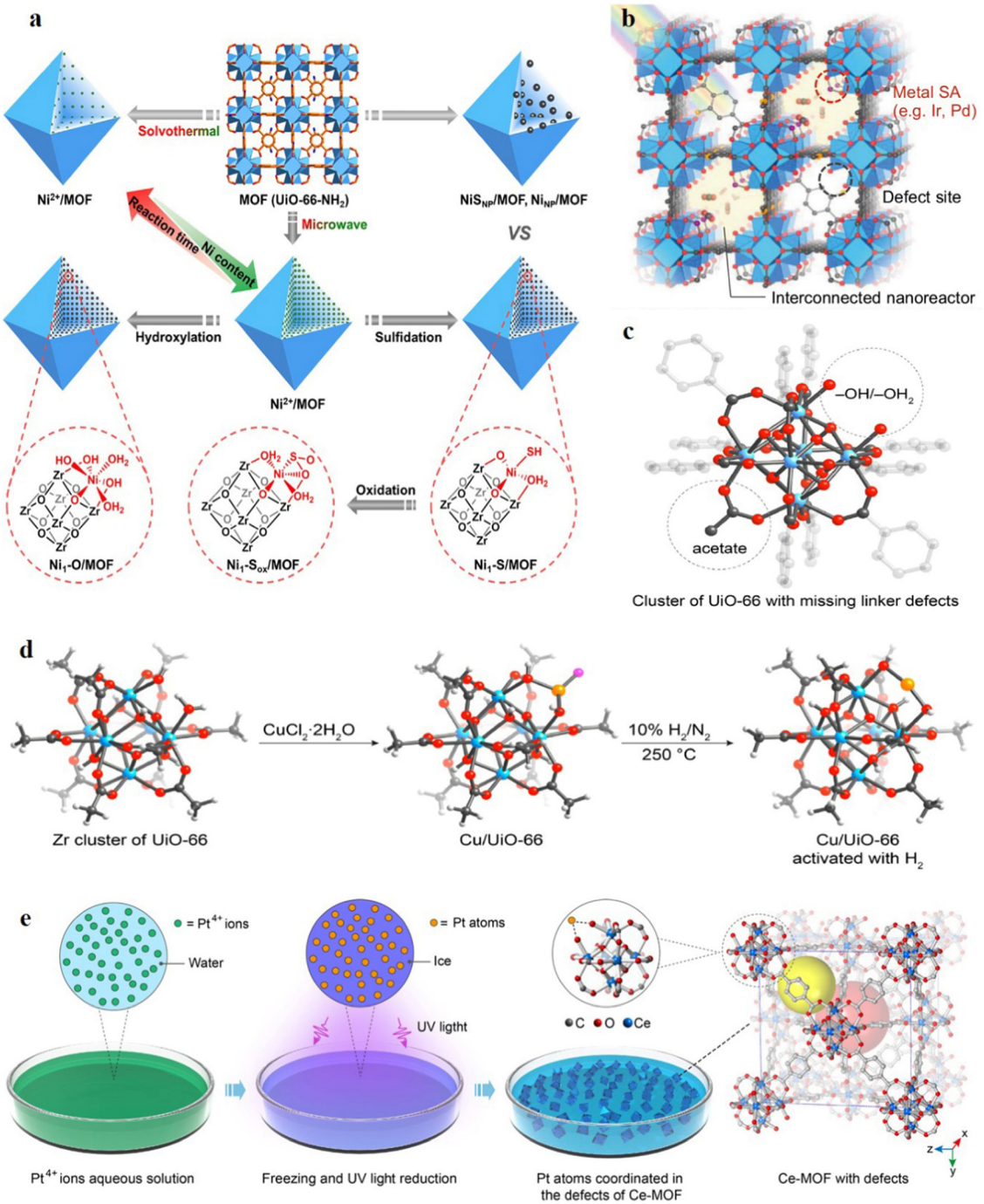

Fig. 4 (a) Schematic illustration of Ni^{2+} decoration in UiO-66-NH_2 *via* a microwave-assisted method and the subsequent coordination environment modulation of Ni SAs to prepare Ni_1–X/MOF, in contrast to the one-pot synthesis of Ni_{NP}/MOF and NiS_{NP}/MOF. Reproduced with permission from ref. 70. Copyright 2021, American Chemical Society. (b) Schematic illustration showing specific single metal atoms (*e.g.*, Ir and Pd) precisely anchored on the edges of the $Zr_6O_4(OH)_4(-CO_2)_{12-x}$ octahedra by controllable defect-engineering. Reproduced with permission from ref. 101. Copyright 2021, Nature Publishing Group. Schematic illustration of (c) the Zr oxo cluster of UiO-66 with $-OH/-OH_2$ and acetate molecules replacing terephthalate linkers and (d) the one-pot synthesis of Cu/UiO-66, prepared by a covalent attachment of Cu SAs to the defect sites at the Zr oxo clusters of UiO-66. Atom labeling scheme: C: black; O: red; Zr: blue; H: light gray. Reproduced with permission from ref. 69. Copyright 2019, American Chemical Society. (e) Schematic illustration of the preparation of the Pt-SA–Ce-MOF catalyst. Reproduced with permission from ref. 87. Copyright 2020, American Chemical Society.

interactions because of the lone pair of electrons on their heteroatoms. In addition, exciton migration in natural photosynthesis occurs mainly in highly ordered porphyrin-like pigments.[102,103] MOFs with highly ordered porphyrins may exhibit antenna-like light-harvesting, and the effective coordination of trapped metal SAs is of increasing interest to

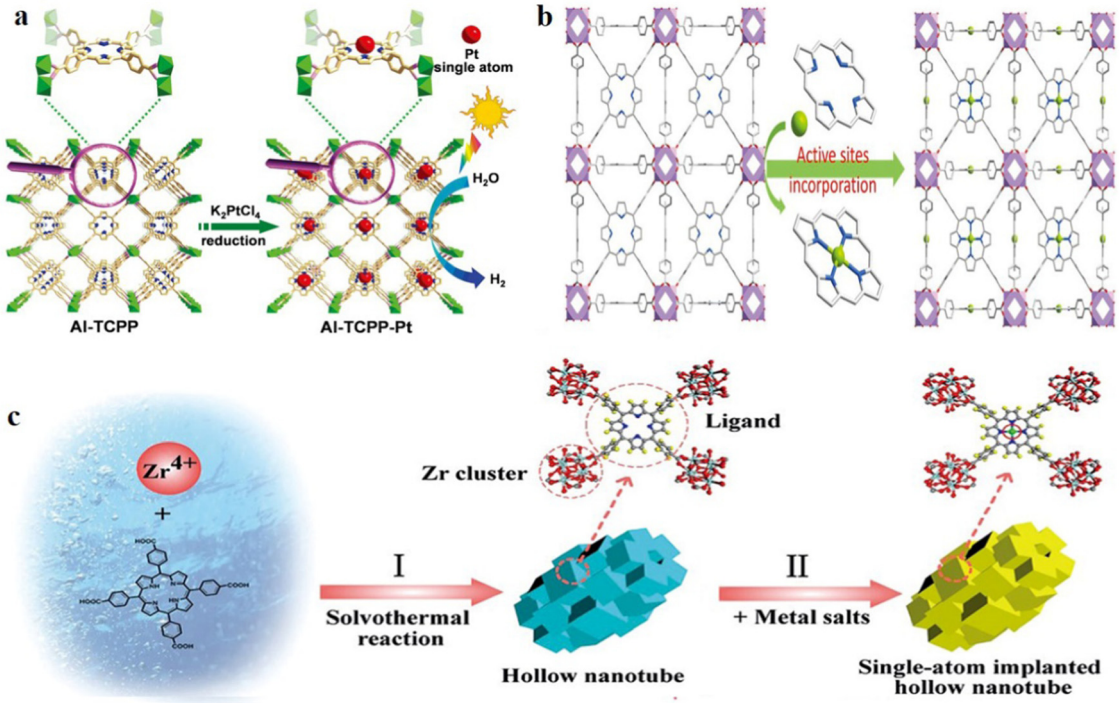

Fig. 5 (a) Schematic illustration showing the synthesis of Al–TCPP–Pt. Reproduced with permission from ref. 68. Copyright 2018, Wiley-VCH. (b) Schematic illustration of the 3D network of MOF-525-Co featuring a highly porous framework and incorporated single Co atoms. Reproduced with permission from ref. 108. Copyright 2016, Wiley-VCH. (c) Schematic illustration of the synthesis of the hollow nanotube MOF and the SA immobilized hollow nanotube MOF. Reproduced with permission from ref. 59. Copyright 2018, Wiley-VCH.

researchers for solar energy conversion.[104–107] Fang *et al.* successfully grew the first highly stable aluminum-porphyrin MOF, Al-TCPP, to stabilize the Pt SAs for efficient hydrogen generation under visible-light irradiation (Fig. 5a).[68] The infinite $Al(OH)O_4$ chains were linked to the porphyrin by self-assembly under hydrothermal conditions at 180 °C to form the highly stable and three-dimensional (3D) microporous MOF Al-TCPP. On the other hand, the Pt SAs in Al-TCPP were obtained by metallization of Pt^{2+} ions onto the porphyrin linker center followed by a simple reduction in a H_2 atmosphere at 180 °C. The Pt SAs achieved by this method were stabilized by intense interactions with the pyrrole-N atoms in porphyrin linkers of Al-TCPP, and the loading rate was determined to be 0.07 wt%. Optical characterization and DFT calculations indicated that the successfully introduced Pt SAs in Al-TCPP could open up efficient electron transfer channels and increase the binding energy of hydrogen, thus significantly improving the hydrogen generation activity. Similarly, Zhang *et al.* reported a similar strategy to implant Co SAs into a Zr–porphyrinic MOF (MOF-525), in which Zr_6 clusters were integrated with the same porphyrin linkers to generate a 3D microporous framework for efficient photocatalysis (Fig. 5b).[108] By heating MOF-525 with cobalt nitrate at 100 °C for 48 h, the unsaturated Co sites were coordinated with the porphyrin units to form a new composite, MOF-525-Co, in which the strong Co–N bonding could effectively avoid aggregation of active Co sites. Designing MOF-supported SACs with hollow nanostructures is conducive to active site exposure and mass diffusion, and is of great interest in the field of photocatalysis. He *et al.*[59] reported a competitive coordination procedure to prepare Zr–porphyrinic hollow MOF nanotubes. Treatment of Zr–porphyrinic hollow MOF nanotubes with $H_2PtCl_6{\cdot}6H_2O$, $IrCl_3{\cdot}xH_2O$, and the porphyrinic linker at 80 °C for 4 h could effectively anchor Pt and Ir ions to form the Pt and Ir SACs (Fig. 5c). Pt and Ir SAs were immobilized on MOFs with a loading of 2.54 and 1.05 wt%, respectively. The Pt SAs were anchored at the atomic level in Zr–porphyrinic hollow MOF nanotubes and four-coordinated by N atoms from porphyrin units. Moreover, this well-defined square-planar porphyrin linker could anchor other noble metal atoms such as Au, Ru, and Pd through this facile synthetic procedure, demonstrating the general applicability of this procedure.

Analogous to the four pyrrole N positions of the organic linker porphyrin unit, ethylenediaminetetraacetic acid (EDTA) can also offer a tetra-linker consisting of two N and two O atoms, which can aggressively bind to single metal ions by a simple trapping process. This is because EDTA is an open chelating linker and features four hard carboxyl groups, two tertiary amines and four carboxyl groups. Li *et al.*[109] successfully incorporated the Pt SAs in the EDTA units of MOF-808-EDTA constructed with EDTA-based linkers and Zr_6 clusters, which was employed in photocatalytic hydrogen generation (Fig. 6a). The successful acquisition of well-defined Pt SAs started with the effective trapping of the single Pt^{2+} ions by the EDTA linker, followed by activation in a hydrogen

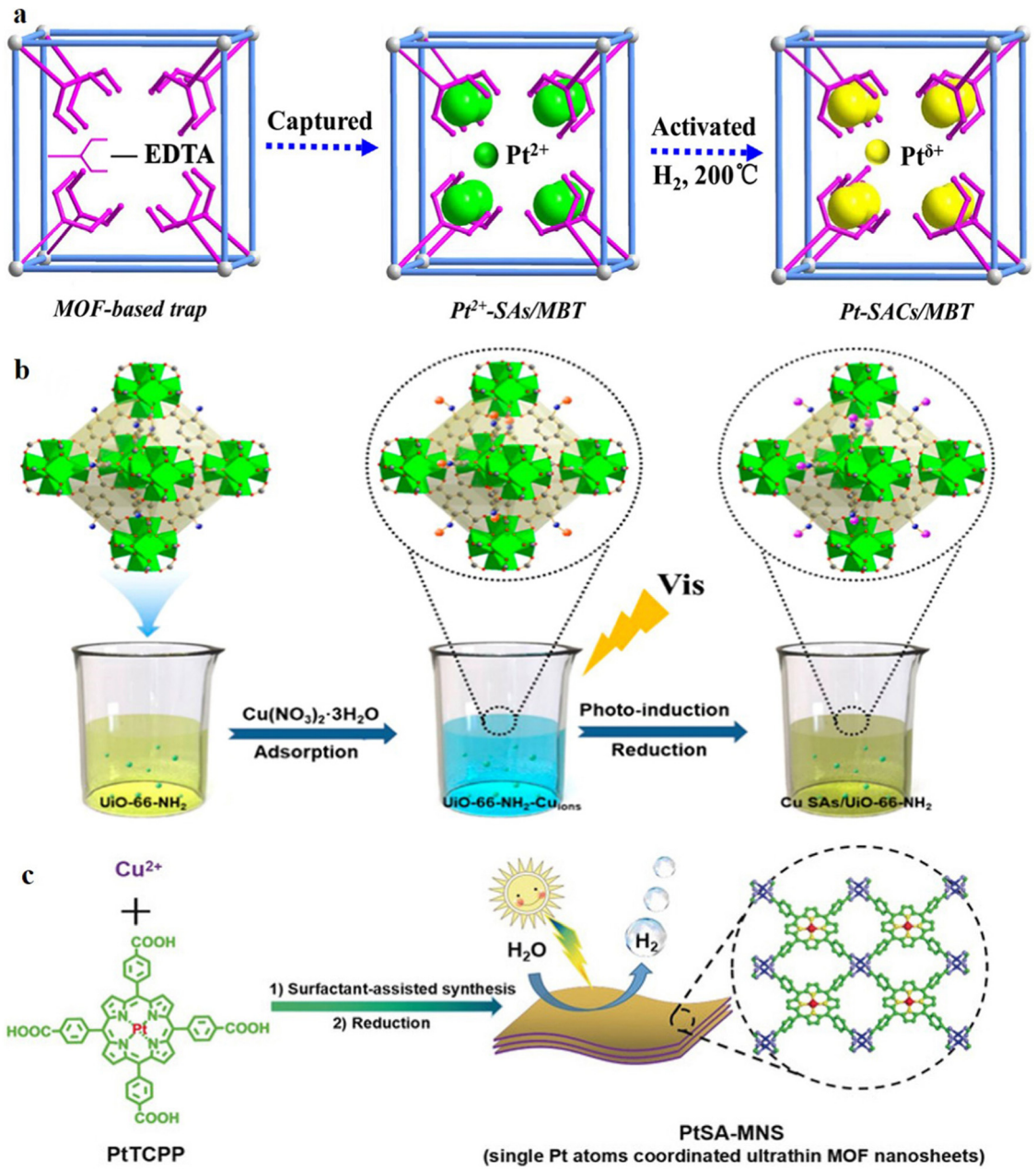

Fig. 6 (a) Schematic illustration of Pt SAs encapsulated in the MOF-808-EDTA *via* the single metal ion trap method. Reproduced with permission from ref. 109. Copyright 2019, Elsevier. (b) Synthesis of the Cu SAs/UiO-66-NH_2 photocatalyst. Zr oxo clusters, C, O and N atoms, Cu ions, and Cu SAs are represented in green, gray, red, blue, orange, and purple. Reproduced with permission from ref. 61. Copyright 2020, American Chemical Society. (c) Schematic illustration of the synthetic route towards Pt SA coordinated ultrathin MOF nanosheets (PtSA-MNSs) through a surfactant-stabilized coordination strategy. Reproduced with permission from ref. 77. Copyright 2019, Wiley-VCH.

atmosphere at 200 °C. In addition, the –NH_2 groups in the organic linkers of the MOF could also be coordinated and immobilized with the Cu SAs. Recently, Wang *et al.* first exploited a photoreduction strategy to anchor Cu SAs on a UiO-66-NH_2 support, which could significantly boost the photoreduction activity of CO_2.[61] In particular, the Cu ions were firstly adsorbed and trapped on the –NH_2 groups of UiO-66-NH_2 and then induced by photoreduction to form the corresponding complexes in the form of SAs (Fig. 6b). It was found that there were strong coordination interactions between isolated Cu atoms and two N atoms in the –NH_2 groups of UiO-66-NH_2.

Ultra-thin two-dimensional (2D) structures can provide a large number of available active sites and minimize the photo-generated carrier travel distance from the interior of the material to the surface, thereby suppressing undesired photo-generated electron–hole recombination. Hence, the preparation of ultra-thin, 2D structured MOFs to support SAs may be desirable for achieving high-level photocatalytic performance. In 2019, Zuo *et al.* first employed a novel surfactant stabilized

coordination route for coordinating ultra-high concentrations of Pt SAs onto ultra-thin 2DMOF nanosheets (PtSA-MNSs) for highly efficient photocatalytic hydrogen generation (Fig. 6c).[77] The authors prepared PtSA-MNSs through a bottom-up coordination strategy using PtTCPP as organic linkers and $Cu_2(COO)_4$ paddle-wheel as metal clusters with the help of polyvinyl pyrrolidone surfactant. Following the normal synthetic route, PtTCPP units were coordinated with $Cu_2(COO)_4$ paddle-wheel metal clusters to construct MOF structures. However, it was important to note that the addition of polyvinyl pyrrolidone could break this conventional synthesis consequence and played an important role in the synthesis of 2D MOFs. The polyvinyl pyrrolidone molecules could selectively attach to the formed MOF surfaces, thus significantly alleviating their buildup and leading to anisotropic growth of the MOFs in the 2D direction, resulting in ultrathin PtSA-MNSs. The Pt SAs can be well-dispersed on the MOF surface with an ultrahigh loading rate of 12.0 wt%. This was because the Pt SAs were coordinated with the porphyrin ring of the organic linker and directly participated in the synthesis of MOFs, thus allowing the MOFs to be loaded with highly dispersed Pt SAs. Such a large number of Pt SAs could serve as electron traps and active sites for the reduction of protons. With the unique advantages of 2D MOFs, efficient hydrogen generation activity could be achieved.

Based on these advances, it can be briefly concluded that the metal clusters and organic linkers in pristine MOFs can provide abundant chelation sites for the construction of SACs (Ni, Pt, Co, Cu, *etc.*). Such high chelation sites of MOFs could firmly and effectively trap SAs with uniform distribution and high loading. Currently, the research on pristine MOFs is still at its nascent stage and has concentrated on a few kinds of MOFs, such as Al–porphyrinic-MOF, UiO-66-NH_2, and Zr–porphyrinic-MOF. Innovative design strategies for expanding the types of available MOF supports to afford SACs are well worth further exploration. Moreover, micro/mesoporous hierarchical structure, hollow structure and 2D MOFs as the support platforms for the loading of SAs have enabled high loading and dispersion of SAs, and faster mass transfer and better accessibility to active sites. Accordingly, research in this area is in high demand. Importantly, future directions can be considered in terms of synthetic raw materials, synthetic conditions and synthetic routes to establish multifunctional MOF platforms for the development of effective photocatalysts for important thermodynamic uphill reactions.

3.2. MOF-derived-supported SACs

In high temperature and harsh chemical environments, most MOFs exhibit instability and may suffer from crystal structure collapse. MOFs have been considered as desirable templates for the construction of highly thermally and chemically stable nanostructured carbon that can inherit many advantages of MOF precursors, like structural tailorability and high porosity.[110,111] Accordingly, these MOF derivatives can effectively avoid the relatively low thermal and chemical stability drawbacks of pristine MOFs and are stable in solution for catalysis, especially under harsh conditions.[112] This has attracted a great deal of attention from scientists with a focus on the possibility of MOF-derived carbon material supported SACs.[113,114] Due to the abundance and uniform distribution of organic linkers in MOFs, the MOF-derived support obtained by pyrolyzing MOFs at high temperature can still act as the N source to form strong metal–N coordination bonds to stabilize SAs.[115] This not only allows the preparation of stable and dispersed SAs, but also greatly improves the thermal and chemical stability of the material. Pyrolysis is an important step in the synthesis of MOF-derived supports, in which the precursors are pyrolyzed *in situ* under high temperature and reducing gas atmosphere conditions. For example, Yan *et al.* reported a facile pyrolysis strategy for supporting SAs in a MIL-125-NH_2-derived N-doped TiO_2/C (N-TC) system (Fig. 7a).[116] The authors were surprised to find that it was possible to indirectly modulate the dispersion state of Ru species on N-TC due to the steadying effect of the non-coordinated $-NH_2$ groups of MIL-125-NH_2 and the inherent pore restriction. When 2% and 5% of Ru^{3+} ions (the rate of Ru/Ti) were injected under a N_2 atmosphere at 800 °C (ramp rate 2 °C min^{-1}, hold 3 h), Ru firmly embedded in N-TC in the single atom state (Ru-SAs@N-TC) and the coexistence of SAs and NPs (Ru-NPs/SAs@N-TC) were observed, respectively. Unpredictably, only 0.457 wt% and 0.360 wt% of Ru were successfully embedded in the corresponding 2% and 5% N-TC supports after pyrolysis. However, the introduction of such a small amount of Ru not only altered the growth of MIL-125-NH_2 and thus the structure of the resulting pyrolysis product, but also facilitated the generation of Ti^{3+}–O_v defects. Compared to Ru NPs, the isolated Ru SAs were even more beneficial in generating more Ti^{3+}–O_v defects, thus providing more capture sites to facilitate the separation and conversion of electron–hole pairs. More often, the doped N arising from pyrolysis under a N_2 atmosphere could also introduce structural defects. The abundance of defect sites generated by Ru and doped N would lead to the modulation of the surface and electronic structures, thus favoring the adsorption energy of the photocatalytic hydrogen generation process. Recently, Zhang *et al.* reported a bottom-up approach to obtain evenly dispersed Cu SAs on the MIL-125(Ti_v) derived TiO_2 for photocatalytic hydrogen generation.[60] As shown in Fig. 7b, the preparation mechanism of Cu SAs supported on MIL-125(Ti_v) derived TiO_2 was demonstrated. Firstly, the as-prepared MIL-125 acted as a precursor to anchor Cu ions to afford metal-MIL-125 intermediates, which was key to ensuring the uniform distribution of isolated Cu SAs on the final photocatalysts. The isolated Cu SAs were well dispersed on the MIL-125(Ti_v) derived TiO_2 by sintering intermediates at 450 °C for 4 h in air. Finally, the actual Cu SA loading on TiO_2 reached 1.5 wt%, suggesting that this approach not only guaranteed high distribution of Cu SAs, but also achieved a large loading capacity of Cu SAs. More strikingly, this treatment actually led to CuSA–TiO_2 with long-term stability and reproducibility for hydrogen generation under simulated solar light irradiation. The optimized CuSA–TiO_2 not only demonstrated no noticeable decrease in the hydrogen generation rate after six consecutive photocatalytic experiments, but also exhibited similar activity

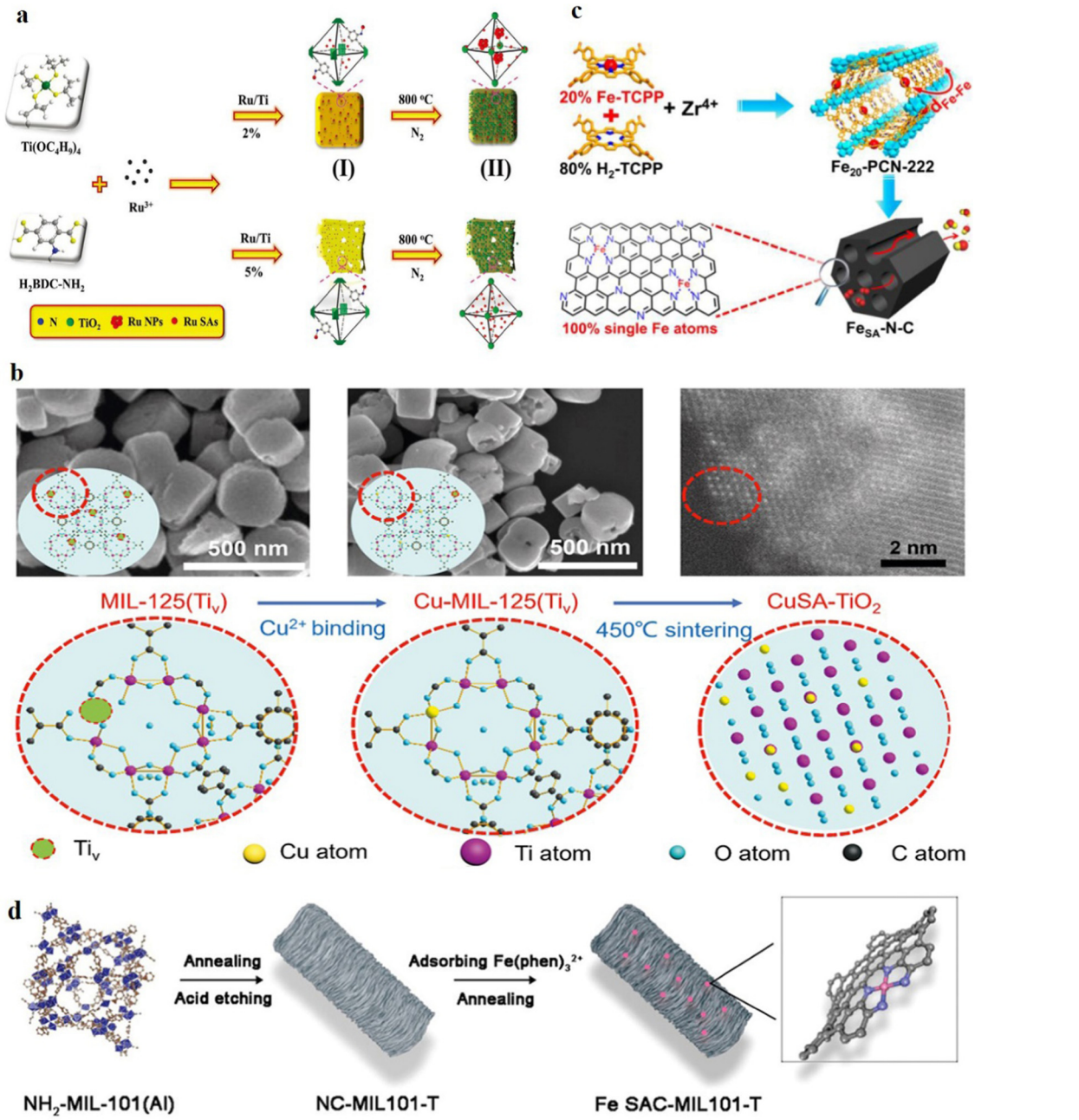

Fig. 7 (a) Schematic illustration of preparation of Ru-NPs/SAs@N-TC and Ru-SAs@N-TC samples. Reproduced with permission from ref. 116. Copyright 2020, Wiley-VCH. (b) Schematic illustration of the formation of copper SAs in the Ti lattice of TiO_2, together with the related images. Reproduced with permission from ref. 60. Copyright 2022, Nature Publishing Group. (c) Schematic illustration of the rational fabrication of the Fe SA-involved FeSA-N-C catalyst *via* a mixed-ligand strategy. Reproduced with permission from ref. 117. Copyright 2018, Wiley-VCH. (d) Schematic illustration of the preparation of Fe SAC-MIL101-T. Reproduced with permission from ref. 118. Copyright 2021, Wiley-VCH.

during the long-term experiment lasting 20 days. Notably, the optimized CuSA–TiO_2 maintained the same photocatalytic activity for water splitting as the freshly prepared sample after 380 days of storage in the laboratory, holding great potential for practical applications.

From the previous discussion, when the porphyrin backbone in MOFs includes four pyrrolic N sites, it can serve as a coordinating site for constructing SACs. Jiao *et al.* reported a novel mixed-linker strategy to create Fe SA implanted N-doped porous carbon by pyrolyzing Fe_x-PCN-222 with Zr clusters as clusters and FeTCPP and H_2TCPP in different ratios as the mixed organic linkers (Fig. 7c).[117] A series of Fe_x-PCN-222 were obtained by adjusting the ratio between FeTCPP and H_2TCPP using porphyrinic PCN-222 as a precursor. Subsequently, Fe_x-PCN-222 was pyrolyzed at 800 °C with an optimized ratio of FeTCPP and H_2TCPP to synthesize Fe_x-PCN-222 porous carbon. By virtue of this mixed-linker strategy, the mixed porphyrin linkers with and without Fe elongated the spatial

distance of Fe^{3+} ions in the MOF skeleton. It effectively inhibited the aggregation of Fe during pyrolysis, resulting in a high loading rate (1.76 wt%) of Fe SAs over Fe_x-PCN-222-derived porous carbon. Notably, the Fe SA implanted Fe_x-PCN-222-derived porous carbon retained a highly ordered hierarchical mesoporous structure during the synthesis, which benefited mass transfer and accessibility of active sites. In addition to organic linkers and metal clusters that could anchor metal ions, pore space within MOFs could also be used to confine organometal species for the immobilization and preparation of SACs. For instance, Xie *et al.* successfully encapsulated a Fe(II)-phenanthroline complex in MIL-101-NH_2 (Al) with a mesoporous cage architecture to acquire FeN_x single atom sites supported by MIL-101-derived mesoporous carbon (Fig. 7d).[118] The MIL-101-NH_2(Al) precursor was pyrolyzed into a series of MIL-101-NH_2 derived materials at 800–1100 °C under a N_2 atmosphere. Then, the products were etched in dilute hydrochloric acid to remove the amorphous Al species and obtain N-doped carbon materials. After acid etching, the N-doped carbon materials with abundant mesopores adsorbed $Fe(phen)_3^{2+}$ complexes internally and externally, and following a second high-temperature pyrolysis treatment (N_2 atmosphere at 800 °C) afforded uniformly dispersed FeN_x single atom sites supported by MIL-101-derived mesoporous carbon materials.

In the field of photocatalysis, MOF-derived-supported SACs have shown excellent photocatalytic activity as well as several advantages over other carbon-supported SACs: (a) the microporosity and morphology of the MOF-derived carbon support can be conveniently controlled by the MOF precursors; (b) SAs have strong interactions with functional groups on the targeted MOF organic linkers and can be firmly embedded on MOF-derived carbon supports, even under harsh synthetic conditions; and (c) by choosing suitable organic linkers of MOFs and the synthesis conditions, heteroatoms can be easily doped in a controlled structure. It has been shown above that MOF-derived carbon materials are one of the promising monoatomic support materials with large specific surface area, adjustable porosity and strong stabilization for SAs. However, it is worth noting that there are still some challenges in the synthesis and application of MOF-derived carbon that deserve further exploration. Pyrolysis is by far the most widely used and facile method for the preparation of MOF-derived-supported SACs. The carbonization temperature and synthesis conditions should be optimized to achieve high stability, good dispersion and high yields of SAs in MOFs. Furthermore, fast, simple, high yielding and environmentally friendly synthesis strategies should be actively sought to cater for the promising future application of MOF-derived-supported SACs in practice.

4. Characterization of MOF-supported SACs

A thorough comprehension of the morphological, electronic, and local coordination structures of SAs at the atomic level is instrumental in finding the optimal balance between composition, structure and photocatalytic activity, which in turn leads to precise and rational modulation of the photocatalytic activity of the MOF-supported SAC photocatalyst.

Traditional measurements (transmission electron microscopy (TEM) and scanning electron microscopy (SEM)) cannot meet the accuracy requirement to directly see the presence of SAs on MOFs.[16] At present, one of the most powerful and advanced techniques available is the high-angle annular dark-field scanning transmission electron microscopy (HAADF-STEM) measurement, which can directly discern and verify the atomic dispersion of SAs in MOFs supports.[119–121] Therefore, this measurement with high resolution and image visualization is commonly and widely employed to identify individual heavy atoms in the MOF supports.[122,123] The intensity of the HAADF-STEM image is proportional to the square of the atomic number, *i.e.*, the brighter parts of the image indicate the presence of higher atomic numbers.[124] Fang *et al.* applied this technique to detect the presence of Pt in the form of Al–TCPP–0.1 Pt, which was not observed by TEM because of its resolution limit (Fig. 8a and b).[68] The authors believed that these bright spots correspond to ultra-small Pt SAs of 0.1 or 0.2 nm, which were uniformly dispersed within Al–TCPP–0.1Pt. The intensity profile in the red-circle region demonstrated that the isolated Pt SAs were separated from each other at a distance of approximately 0.5 nm. With increasing Pt content (Al–TCPP–0.3Pt), the HAADF-STEM images clearly showed the appearance of Pt SAs and a small number of Pt clusters with slight Pt aggregation occurring; however, this was not observed in the TEM images with obvious particles. In another case, Zhang *et al.* obtained HAADF-STEM images to investigate the structure of Cu SAs supported on MIL-125(Ti_v) derived TiO_2, and the presence of atomically dispersed Cu SAs exclusively presenting in the Ti vacancies was clearly confirmed by HAADF-STEM (Fig. 8c and d).[60] In summary, HAADF-STEM can provide clearer images to confirm the distribution of SAs on MOF supports and is a more powerful technique than conventional electron microscopy for providing structural information of localized areas. However, it can only give information about SAs in a particular field, resulting in a possible misinterpretation of the results obtained. Therefore, combining HAADF-STEM with other characterization techniques is of great importance for the comprehension of SACs.

To further obtain more overall and detailed structural information based on the local atomic structure, chemical state and coordination environment of MOF-supported SACs, X-ray absorption spectroscopy (XAS) has become a commonly available tool in recent years.[125] Specifically, XAS can be generally divided into X-ray absorption near-edge spectroscopy (XANES) and extended X-ray absorption fine structure (EXAFS) spectroscopy.[126] While XANES mainly provides information on the valence state and coordination chemistry around the target metal species, EXAFS prefers to probe the local structure of the target metal species in terms of its coordination to surrounding atoms.[127,128] EXAFS measurements to characterize the metal–metal coordination number can be used to effectively identify whether SACs are successfully obtained.[113] According to the definition of SAs, metal–metal bonds are not present in the active species in EXAFS.

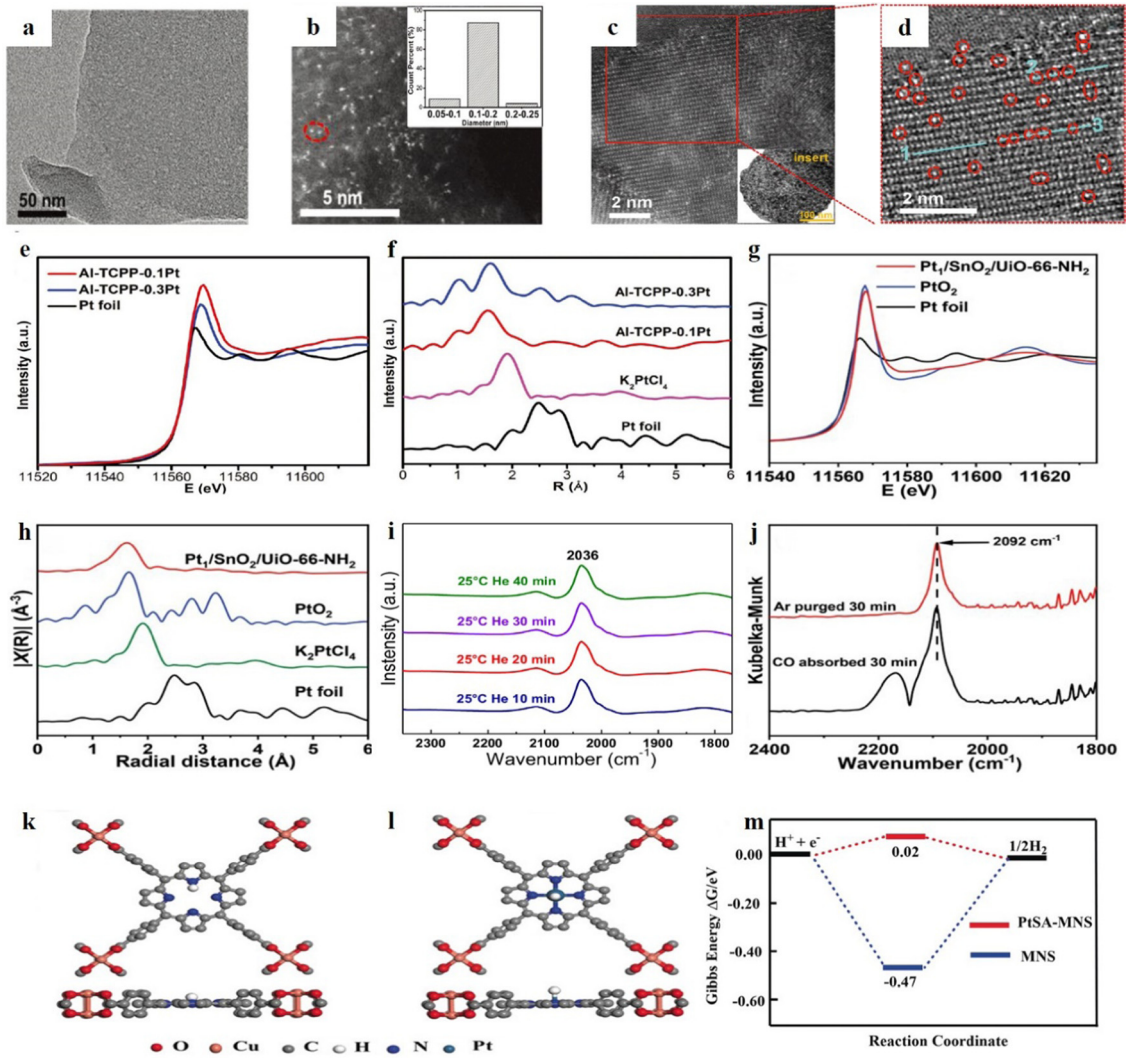

Fig. 8 (a) Transmission electron microscopy and (b) HAADF-STEM images of Al–TCPP–0.1Pt. Reproduced with permission from ref. 68. Copyright 2018, Wiley-VCH. (c) HAADF-STEM image of CuSA–TiO_2. (d) Filtered HAADF-STEM image of the area highlighted with a red rectangle in (c) and the corresponding line scan profiles. Reproduced with permission from ref. 60. Copyright 2022, Nature Publishing Group. (e) The normalized XANES spectra at the Pt L_3-edge of Al–TCPP–0.3Pt, Al–TCPP–0.1Pt, and Pt foil. (f) Fourier transformed EXAFS spectra of Al–TCPP–0.3Pt, Al–TCPP–0.1Pt, K_2PtCl_4, and Pt foil. Reproduced with permission from ref. 68. Copyright 2018, Wiley-VCH. (g) The Pt L_3-edge XANES spectra for $Pt_1/SnO_2/UiO\text{-}66\text{-}NH_2$, PtO_2, and Pt foil. (h) Fourier transformed EXAFS spectra for $Pt_1/SnO_2/UiO\text{-}66\text{-}NH_2$, PtO_2, K_2PtCl_4 and Pt foil. Reproduced with permission from ref. 78. Copyright 2021, Wiley-VCH. (i) DRIFT spectra of CO adsorbed on Pt-SACs/MBT after being purged with He gas for different time lengths. Reproduced with permission from ref. 109. Copyright 2019, Elsevier. (j) DRIFT spectra of CO adsorbed on $Pt_1/SnO_2/UiO66\text{-}NH_2$ before and after being purged with Ar gas for 30 min. Reproduced with permission from ref. 78. Copyright 2021, Wiley-VCH. Schematic illustration of the structural models for H* adsorbed on (k) MNSs and (l) PtSA-MNSs, and (m) ΔG_{H^*} on MNSs and PtSA-MNSs, respectively. Reproduced with permission from ref. 77. Copyright 2019, Wiley-VCH.

Therefore, if the EXAFS data do not include any information about the metal–metal bond, it can basically be inferred that only SAs are present in the catalyst. Fang *et al.* first observed the electronic structure of Pt with the help of XANES analysis.[68] The white line peak in Al–TCPP–0.1Pt corresponded to the electronic transition of Pt from the $2p_{2/3}$ to the unoccupied 5d state and showed a significantly high intensity, which was slightly lower in Al–TCPP–0.3Pt, but both were higher than the intensity of the Pt foil (Fig. 8e). The authors suggested that the electronic structure of Pt in Al–TCPP–0.1Pt was more oxidized, while the valence state of Pt in Al–TCPP–0.3Pt was lower. Furthermore, EXAFS was performed to obtain more information on the local structure of Pt, and the results showed a prominent Pt–N contribution peak at ≈1.5 Å in Al–TCPP–0.1Pt, with no significant Pt–Cl (≈1.9 Å) or Pt–Pt bond peak, confirming that Pt SAs were coordination-stabilized to N atoms, and that a few (or very few) Pt particles or clusters were present in Al–TCPP–0.1Pt (Fig. 8f). In another case, Sui *et al.* revealed the local coordination environment of isolated Pt SAs in $Pt_1/SnO_2/UiO\text{-}66\text{-}NH_2$ by XAS characterization.[78] The XANES profiles of Pt K-edge for $Pt_1/SnO_2/UiO\text{-}66\text{-}NH_2$ indicated that the Pt atoms were highly oxidized (Fig. 8g). Fourier-transform extended EXAFS of $Pt_1/SnO_2/UiO\text{-}66\text{-}NH_2$ indicated only one major peak at about 1.63 Å, which was assigned to the Pt–O contribution, while no obvious Pt–Pt (≈2.49 Å, Pt foil)

or Pt–Cl (≈1.9 Å, K_2PtCl_4) peaks were detected. The EXAFS fitting curve revealed that isolated Pt atoms were coordinated to about 4 oxygen atoms. The overall results indicated that the Pt species in Pt_1/SnO_2/UiO-66-NH_2 were present in the form of isolated SAs and were coordinated to about 4 oxygen atoms with atom distances of about 1.63 Å (Cu–O) (Fig. 8h). These studies demonstrate that operando XAS characterization can be performed alongside HAADF-STEM characterization to further provide a complete picture to confirm the atomic dispersion, chemical state and coordination environment of SAs on the MOF support.

In general, diffuse reflectance infrared Fourier transform (DRIFT) spectroscopy is used to investigate the behavior towards the probe molecules based on MOF-supported SAC photocatalyst behavior towards the probe molecule, mainly employing carbon monoxide (CO) as the probe molecule, and is an accessible technology that allows straightforward characterization of SAs.[129,130] In contrast to HAADF-STEM, this allows non-local characterization that can provide solid evidence for the successful formation of SAs. Li *et al.* performed DRIFT measurements on Al–TCPP–0.1Pt and observed only one peak with a symmetric shape centered at 2036 cm^{-1} after purging with He to clear poorly adsorbed CO (Fig. 8i).[109] The authors suggested that CO was linearly chemisorbed on Pt SAs with a uniform structure. The absence of any characteristic peaks in the DRIFT corresponding to linear or bridging adsorption of CO was evidence of the absence of Pt clusters and NPs, further confirming the single atomic dispersion of all Pt species. In particular, the chemisorption peaks of CO maintained their integrity with increasing He purging time, and the authors concluded that the lack of interactions between the adsorbed CO molecules further confirmed the presence of the Pt SAs. In addition, Sui *et al.* applied DRIFT spectra to reveal the oxidation state and dispersion of Pt in Pt_1/SnO_2/UiO-66-NH_2 for photocatalysis (Fig. 8j).[78] After purging with Ar for 30 min, only a strong vibration band at 2092 cm^{-1} (≈2030 cm^{-1} related to CO on Pt^0) caused by single Pt atom linear chemisorption of CO was observed and well retained. The authors suggested that CO adsorbed on $Pt^{\delta+}$ rather than Pt^0 and all Pt species were atomically dispersed in Pt_1/SnO_2/UiO-66-NH_2.

Theoretical calculations have long been regarded as an integral part of experimental science, providing fundamental insight into reaction mechanisms. In recent years, theoretical calculations have become increasingly valuable in the field of catalysis, as DFT calculations provide more detailed information about the catalyst with greater accuracy and in less time. SAs supported on MOFs with coordination environments and well-defined active sites could act as a perfect platform for theoretical modelling. DFT calculations can provide more detailed structural, coordination environment and electronic structure information for SAs supported on MOFs. Furthermore, photocatalytic reactions involve energy barriers, transition states and adsorption energy, and the distribution of products, which are the critical factors influencing the performance of MOF-supported SACs and they can be identified quantitatively by performing DFT calculations. Therefore, DFT calculations are an indispensable tool for determining the configuration, atomic characters and photocatalytic reaction mechanism of MOF-supported SACs.

Abdel-Mageed *et al.* carried out DFT calculations to model Cu/UiO-66 by attaching Cu atoms to defect sites on the Zr_6 clusters of UiO-66 to elucidate the coordination environment of Cu SAs.[69] The experimental findings indicated that isolated Cu atoms were anchored at the atomic level of UiO-66 and were 3-fold coordinated to one chlorine atom and two oxygen atoms in the –OH/–OH_2 defect sites of UiO-66 with atom distances of 2.15 Å (Cu–Cl), 1.89 and 1.95 Å (Cu–O). Moreover, it was found that after H_2 pretreatment, the atomically dispersed 3-fold coordinated Cu species were converted to 2-fold coordinated Cu^+ that bound to –OH/–OH_2 defect sites on the Zr_6 clusters with an atom distance of 1.86 Å (Cu–O), while Cu–Cl was removed (Fig. 4d). Overall, the DFT calculations were consistent with the structural conclusions derived from the EXAFS measurements and further refined the structural information of Cu/UiO-66.

Computational modeling can also be performed to examine the electronic structure of MOF-supported SACs in selective photochemical reactions for studying the distribution of the products. Wang *et al.* developed a photoinduction method to achieve UiO-66-NH_2-supported Cu SACs for photocatalytic reduction of CO_2 to liquid fuels.[61] The authors probed the electronic structure of Cu SAs/UiO-66-NH_2 and pristine UiO-66-NH_2 *via* DFT calculations. The authors concluded that the planar double coordination conformation of Cu with two adjacent –NH_2 groups was the most stable and consistent conformational model for the Cu SAs anchored on the UiO-66-NH_2 support, in good agreement with the XANES results. More importantly, the partial density of states (PDOS) and total density of states (TDOS) revealed that the band gap of Cu SACs/UiO-66-NH_2 was reduced because of the enrichment of electrons from the Cu SAs (electron doping) on Cu SAs/UiO-66-NH_2 compared to the pristine UiO-66-NH_2. Furthermore, the authors studied the thermodynamic aspects to determine the activity and selectivity of Cu SAs/UiO-66-NH_2 toward the photocatalytic reduction of CO_2 to the liquid fuels. The results demonstrated that Cu SAs/UiO-66-NH_2 featured the lowest formation energy to generate CHO* and CO* intermediates, indicating the strongly enhanced photocatalytic reduction activity of CO_2 to methanol and ethanol. In addition, computational models can be used to obtain a fundamental insight into the role of SAs in MOFs, which in turn can be used to underpin the significantly enhanced photocatalytic performance gained from MOF-supported SACs in the experimental results. Zuo *et al.* performed DFT calculations to investigate the contribution of Pt SAs in PtSA-MNSs to significantly enhanced photocatalytic hydrogen generation performance.[77] The density of states analysis demonstrated that PtSA-MNSs and MNSs showed strong and broad visible-light absorption, and the introduction of Pt SAs facilitated the formation of VB states by the generation of a number of new hybridized electronic states. The authors constructed corresponding structural models of H* (atom) adsorption on the surfaces of PtSAC-MNSs and

MNSs (Fig. 8k and l). Notably, PtSAC-MNS showed the most suitable calculated results for the H binding free energy, suggesting the efficient electron–proton process to produce H* and fast hydrogen generation (Fig. 8m). This was consistent with experimental findings that PtSA-MNSs featured the best hydrogen generation performance with respect to the corresponding materials. More importantly, computational modeling is also able to determine the charge transfer paths and their dissipation by modelling the charge density on the metal single atom. Zhang *et al.* established a theoretical model for the CuSA–TiO_2 sample to examine the transfer of photogenerated electrons to the Cu SAs by DFT calculations.[60] The calculations indicated that the charge density around the Cu atom increased significantly with increasing irradiation time, while the charge density on Cu decreased markedly after irradiation stopped. Specifically, photogenerated electrons were accumulated on Cu atoms allowing the reduction of Cu^{2+} to Cu^{+}, while Cu^{+} could be oxidized to Cu^{2+} after turning off the irradiation. Moreover, the authors also investigated the charge density distribution of pristine TiO_2 and the results showed slower charge transfer and lower charge density in pristine TiO_2 compared to the CuSA–TiO_2 sample. Consequently, CuSA–TiO_2 exhibited even better photocatalytic activity.

The rational design of MOF-supported SACs with high activity as well as selectivity is vital for the development of high-performance MOF photocatalysts for utilizing solar energy. In recent years, the development of advanced characterization tools and theoretical calculations has enabled scientists to better explore the structure–activity relationships of MOF-supported SACs during photocatalytic reactions. Accordingly, this in turn allows for the better design of MOF-supported SACs with tailored functionality in specific photocatalytic reactions. Therefore, it is highly desired to design more powerful characterization tools to study MOF-supported SACs, which would provide more detailed information about the effects of SAs on MOFs. More importantly, a more valuable and reasonable theoretical calculation model should be constructed in combination with other characterization techniques to further support the experimental results.

5. Application of MOF-supported SACs in photocatalytic energy conversion

It is evident that the MOFs can be an excellent support to prepare stable SAs with a high metal loading. Conversely, the coordinatively isolated SAs can offer abundant unsaturated active sites on the surfaces of photocatalysts to elevate the process of photocatalytic reactions. More advantageously, the decoration of isolated SAs on MOFs could simultaneously enhance the light-harvesting capability and boost the charge separation/transfer during photocatalytic reaction. Thereafter, the MOF-supported SAC photocatalysts can naturally achieve efficient photocatalysis. In this section, we will discuss the MOF-supported SAC photocatalysts in the field of photocatalysis related to CO_2 photoreduction and hydrogen generation (Table 1).

5.1. CO_2 photoreduction

Global warming and global energy demand have driven widespread attention to the sustainable reduction of CO_2 into value-added carbon products.[131] Based on the concept of biomimetic design of natural photosynthesis processes, photocatalytic reduction of CO_2 is a remarkably valuable route for solar-to-energy conversion.[132,133] SAs (*e.g.*, Ni, Co, Fe, Cu, Zn) supported on MOFs are considered as efficient photocatalysts for CO_2 reduction, both theoretically and experimentally. For instance, Wang *et al.* incorporated isolated Cu SAs into UiO-66-NH_2 (Cu SAs/UiO-66-NH_2) for the solar-to-energy conversion of CO_2 to ethanol and methanol, which achieved remarkable activity, with a generation rate of 4.22 and 5.33 μmol h^{-1} g^{-1}, respectively.[61] The formation of isolated Cu SAs on the UiO-66-NH_2 matrix was identified from the HAADF-STEM image, where the isolated Cu atoms were clearly visible from the bright spots (Fig. 9a). Fourier-transformed EXAFS spectra further verified the existence of Cu SAs with Cu–N and no presence of Cu–Cu bonds. By employing time-resolved photoluminescence spectra, the lifetime of the photogenerated charge carriers in Cu SAs/UiO-66-NH_2 was calculated to be τ_{avg} = 6.53 ns, while in UiO-66-NH_2 it was calculated to be τ_{avg} = 4.91 ns (Fig. 9b). Obviously, the τ_{avg} values reflected the electron capture capability of samples, and the remarkably prolonged τ_{avg} of Cu SAs/UiO-66-NH_2 suggested that Cu SAs/UiO-66-NH_2 possessed a slower photogenerated charge carrier recombination rate. A faster interface charge transport found on Cu SAs/UiO-66-NH_2 could be also confirmed by photoelectrochemical experiments. Owing to the above-mentioned advantages, the photocatalytic performance of Cu SAs/UiO-66-NH_2 was strongly enhanced compared to that of UiO-66-NH_2 toward ethanol and methanol production. Moreover, based on DFT calculations, they fully explored the electronic structure of Cu SAs/UiO-66-NH_2 and formation energies of intermediates (CO* and CHO*) for CO_2 photoreduction. They revealed that isolated Cu SAs on UiO-66-NH_2 could favor electron enrichment on Cu SAs/UiO-66-NH_2 and greatly reduce the formation barriers of both CO* and CHO*. Rapidly produced CO* and CHO* were readily coupled at the Cu site to form ethanol.[134] Specifically, in Cu SAs/UiO-66-NH_2, the photogenerated electrons could be transferred from the H_2BDC-NH_2 linker to the Zr oxo cluster under visible-light irradiation. Then, the isolated Cu atoms would capture photogenerated electrons and serve as active sites to induce activation of CO_2 absorbed on the UiO-66-NH_2 support (Fig. 9c). Eventually, Cu SAs/UiO-66-NH_2 achieved remarkably improved activity and selectivity for multielectronic conversion of CO_2 to ethanol and methanol. Importantly, after four cycles, Cu SAs/UiO-66-NH_2 showed no visible change in photocatalytic activity and crystal structure, indicating that Cu SAs/UiO-66-NH_2 photocatalysts featured high durability and would be suitable for the practical application of photocatalytic CO_2 reduction (Fig. 9d).

Cobalt-metalated porphyrin-based materials have received much attention for their highly efficient and selective performance in CO_2 photoreduction and visible-light utilization. For example, Zhang *et al.* successfully developed a Co-porphyrin MOF, termed MOF-525-Co, which exhibited significantly

Table 1 Summary of MOF-based supported SACs for photocatalytic energy conversion[a]

Photocatalysts	Metal configuration	Metal loading (wt%)	BET ($m^2\ g^{-1}$)	Reaction	Photoactivity	Reaction conditions	Stability	Ref.
Cu SAs/ UiO-66-NH_2	Cu–N_2	0.39	—	The conversion of CO_2 to CH_3OH and C_2H_5OH	5.33 μmol g^{-1} h^{-1} (CH_3OH), 4.22 μmol g^{-1} h^{-1} (C_2H_5OH)	0.1 g of photocatalyst, 50 mL of H_2O and 0.1 mL of TEOA, 300 W Xe lamp, $\lambda > 400$ nm	Four	61
MOF-525-Co	Co–N_4	6.01	1317	The conversion of CO_2 to CO and CH_4	200.6 μmol g^{-1} h^{-1} (CO), 36.76 μmol g^{-1} h^{-1} (CH_4)	2 mg of photocatalyst, 2 mL of solution (acetonitrile/TEOA = 4 : 1), 300 W Xe arc lamp, 800 nm $> \lambda >$ 400 nm	Three	108
Ir_1/A-aUiO membranes	Ir–$O_{3.8}$	1.4	—	The conversion of CO_2 to HCOOH	3.38 mmol g^{-1} h^{-1}	15 mg of photocatalyst, 50 mL of solution (water/isopropanol = 4 : 1), 300 W Xe lamp, $\lambda > 420$ nm	Long-term operation (100 h)	101
Al–TCPP–0.1Pt	Pt–$N_{3.5}$	0.07	—	Hydrogen generation	129 μmol g^{-1} h^{-1}	5 mg of photocatalyst, 20 mL of solution (acetonitrile/water/TEOA = 18 : 1 : 1), 300 W Xe lamp, $\lambda > 380$ nm	Four	68
HNTM-Ir/Pt	Pt–$N_{2.2}Cl_{3.8}$	1.05 (Ir); 2.54 (Pt)	844	Hydrogen generation	201.9 μmol g^{-1} h^{-1}	50 mg of photocatalyst, 50 mL of solution (acetonitrile/water/TEOA = 45 : 1 : 4), 300 W Xe lamp, $\lambda > 400$ nm	Three	59
PtSA-MNSs	Pt–$N_{3.6}$	12	570	Hydrogen generation	11 320 μmol g^{-1} h^{-1}	5 mg of photocatalyst, 50 mL of water with 0.1 M ascorbic acid, 300 W Xe lamp, $\lambda > 420$ nm	Long-term operation (18 h)	77
Ru-NPs/ SAs@N-TC	—	0.457	307.5	Hydrogen generation	100 μmol h^{-1}	20 mg of photocatalyst, 100 mL of water with 20 mL of methanol, 300 W Xe lamp, 780 nm $> \lambda >$ 320 nm	Three	116
Ni_1–S/MOF	Ni–$S_{1.0}O_{3.3}$	4.76	—	Hydrogen generation	1360 μmol g^{-1} h^{-1}	5 mg of photocatalyst, 4 mL of DMF, 100 μL of water, 1 mL of TEOA, and two drops of DMSO, 300 W Xe lamp, $\lambda > 380$ nm	Six	70
Pd_{10}@Pt_1/ UiO-66-NH_2	Pt–$O_{0.8}$-$Pd_{6.1}Zr_{3.6}$	0.12	—	Hydrogen generation	1200.5 μmol g^{-1} h^{-1}	3 mg of photocatalyst, 27 mL of acetonitrile with 0.2 mL of water and 3 mL of triethylamine, 300 W Xe lamp, $\lambda > 380$ nm	Five	143
Pt_1/SnO_2/ UiO-66-NH_2	Pt–$O_{3.9}$	1.35	—	Hydrogen generation	2167 μmol g^{-1} h^{-1}	5 mg of photocatalyst, 4.5 mL of acetonitrile, 100 μL of water, 0.5 mL of TEOA, 300 W Xe lamp, $\lambda > 380$ nm	Three	78
CuSA–TiO_2	Cu–O	~1.5	294	Hydrogen generation	101.74 mmol g^{-1} h^{-1}	20 mg of photocatalyst, 120 mL of solution (methanol/water = 2 : 1), 500 W Xe lamp	Storage for 380 days and reaction for 6 cycles (30 h)	60

[a] Abbreviations: BET = Brunauer–Emmett–Teller specific surface area; TEOA = triethanolamine; — = not available; SA = single atom; DMF = *N*,*N*-dimethylformamide; DMSO = dimethyl sulfoxide; A-aUiO = activated UiO-66-NH_2.

enhanced photocatalytic conversion of CO_2 with high CO (200.6 mmol g^{-1} h^{-1}) and CH_4 (36.67 mmol g^{-1} h^{-1}) evolution rates.[108] MOF-525-Co featured Zr as metal nodes and the active Co sites were implanted and atomically dispersed in porphyrin rings, which facilitated the adsorption and activation of CO_2 (Fig. 5b). By analyzing wavelet transform EXAFS, it was found that Co species were trapped by MOF-525 in the presence of Co–N bonds and existed as mononuclear centers (Fig. 9e). The Co K-edge XANES spectrum of MOF-525-Co further validated that the Co species were mainly present in the form of Co–N species instead of Co–Co bonds in MOF-525-Co. Compared with the parent MOF, MOF-525-Co showed a substantial enhancement in CO (200.6 μmol g^{-1} h^{-1}) and CH_4 (36.76 μmol g^{-1} h^{-1}) yields of 3.13-fold and 5.93-fold, respectively. The source of CO and CH_4 products produced was confirmed by gas chromatography and mass spectra, and the results indicated that both CO and CH_4 products certainly originated from CO_2 rather than other carbon substances in this system. *In situ* Fourier transform infrared (FTIR) and charge transfer efficiency investigations directly revealed that the greatly enhanced photocatalytic activity of MOF-525-Co could be ascribed to the strong CO_2 adsorption ability over active Co sites and the boosted charge separation efficiency in porphyrin units after Co SA introduction. Accordingly, CO_2 could be easily captured and subsequently photocatalytically reduced into CO and CH_4 by energetic electrons at the active Co sites. The charge transfer route of MOF-525-Co in

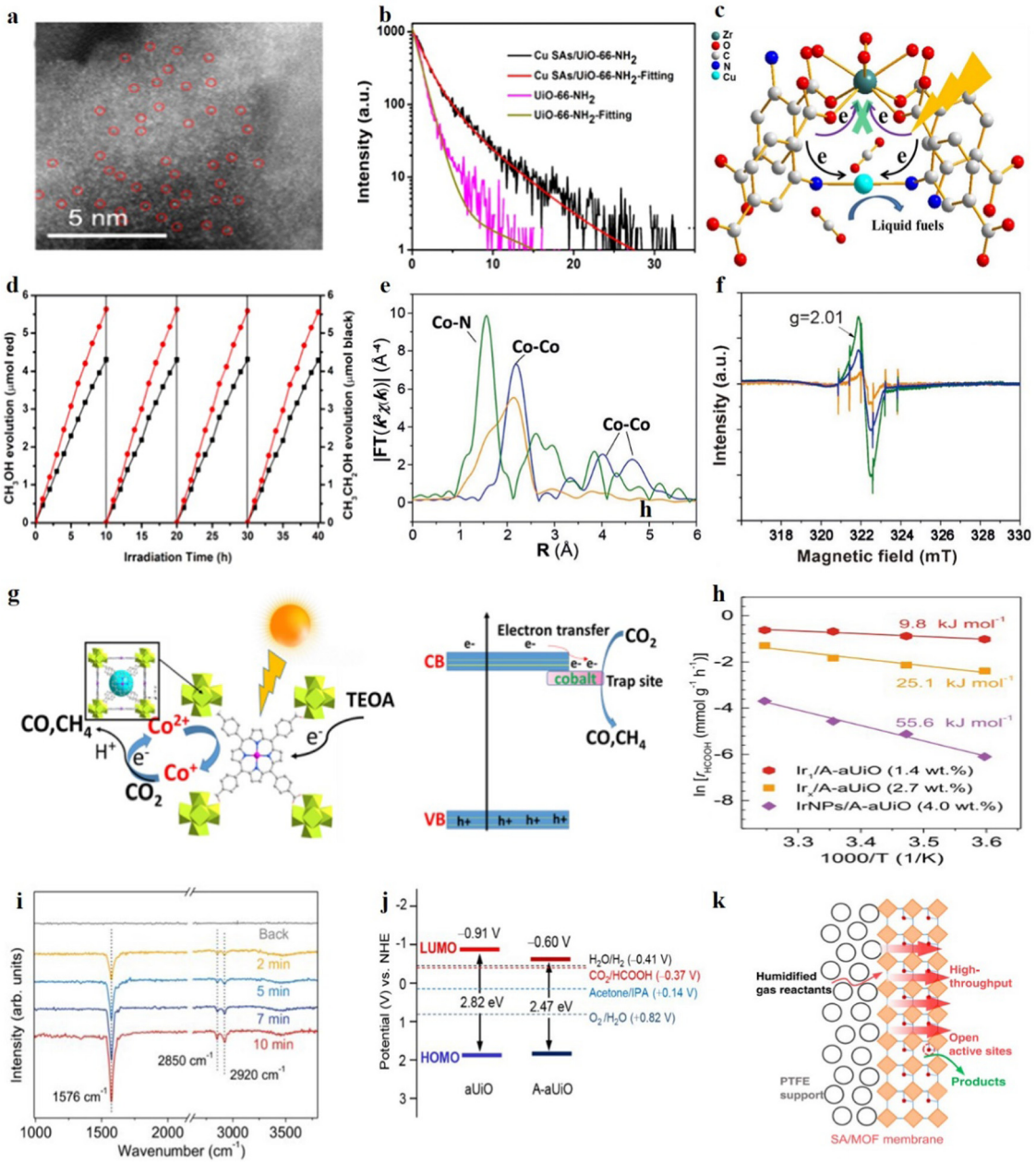

Fig. 9 (a) HAADF-STEM images for Cu SAs/UiO-66-NH_2. (b) Time resolved fluorescence spectra and fitting results of Cu SAs/UiO-66-NH_2 and UiO-66-NH_2. (c) Schematic illustration of the mechanism of photocatalytic CO_2 reduction over Cu SAs/UiO-66-NH_2. (d) Cyclic tests of Cu SAs/UiO-66-NH_2 upon visible-light irradiation. Reproduced with permission from ref. 61. Copyright 2020, American Chemical Society. (e) Fourier-transform EXAFS spectra for MOF-525-Co. (f) ESR spectra of MOF-525-Co under light and CO_2 (purple), light and N_2 (orange), and N_2 (green). (g) Schematic illustration of the mechanism of photocatalytic CO_2 reduction over MOF-525-Co. Reproduced with permission from ref. 108. Copyright 2016, Wiley-VCH. (h) Schematic of apparent activation energy of various photocatalysts for HCOOH generation. (i) *In situ* FTIR spectra of A-aUiO and Ir_1/A-aUiO upon irradiation for different time periods. (j) Schematic illustration of the CO_2/HCOOH reduction potential, and the band gap energies of A-aUiO and aUiO. (k) Schematic illustration of humidified CO_2 gas fed through the membrane in the gas–membrane–gas mode. Reproduced with permission from ref. 101. Copyright 2021, Nature Publishing Group.

the CO_2 adsorption and activation process was revealed through electron spin resonance (ESR) spectroscopy (Fig. 9f). With visible-light irradiation, the signal intensity assigned to Co^{2+} was greatly weakened, suggesting the optically induced valence reduction of Co^{2+} to Co^{+} owing to the acceptance of photo-generated electrons on the Co atoms. Subsequently, the ESR signal of Co^{2+} was in turn enhanced along with the introduction of CO_2 into the system, suggesting that Co^{+} were partially oxidized back into Co^{2+} during the CO_2 photocatalytic reduction. Moreover, the signal of Zr^{3+} was found in MOF-525 but nearly disappeared in MOF-525-Co under visible-light irradiation, indicating that the effective electron transfer from the linker to the

Co center greatly limited the electron transfer from the porphyrin linker to the Zr oxo cluster. Accordingly, as shown in Fig. 9g, these results indicated that photogenerated electrons could be transferred from the porphyrin linkers to coordinatively unsaturated Co centers, which could serve as photocatalytically active sites for the activation of CO_2 molecules. Moreover, the results of three cycles of photocatalytic CO_2 reduction experiments confirmed the stable photocatalytic activity of MOF-525-Co. The Ru sites in the atomically dispersed Ru-polypyridine complexes possessed strong visible-light collection ability and a long excited state lifetime, and their incorporation into the linkers of MOFs has been demonstrated to be a valid strategy for improving photocatalytic properties. For example, Mahmoud *et al.* incorporated $Ru(cptpy)_2$ sites into AUBM-4, and the modified AUBM-4 framework showed high efficiency and stability for the conversion of CO_2 to formate which was driven by visible light. The AUBM-4 crystals retained their high crystallinity after 1 week of suspension in water.[135] In a photocatalytic CO_2 reduction system using triethanolamine (TEOA) as a sacrificial electron donor, AUBM-4 delivered a formate yield rate of 366 μmol g^{-1} h^{-1} along with excellent recyclability and no significant activity loss after four consecutive cycles. Incorporation of $Ru(cptpy)_2$ as the linkers of AUBM-4 led to a long emission lifetime and facile multielectron injection from photoexcited $cptpy^{\bullet-}$ to CO_2, thus achieving efficient conversion of CO_2.

However, the photoreduction of permanent gaseous CO_2 to liquid fuels at the heterogeneous reaction interface suffers from slow mass transfer at the gas–liquid–solid boundary, which severely hampers subsequent catalytic kinetics. Combining the advantages of SAs and porous MOF substrates, Hao *et al.* successfully incorporated single iridium (Ir_1) atoms at the clusters of gas-permeable MOF membranes (UiO-66-NH_2), which showed desirable photocatalytic performance in CO_2 reduction to HCOOH under mild conditions and visible-light irradiation (Fig. 4b).[101] Related characterization experiments revealed that Ir_1 SAs were immobilized on the metal clusters of defect-engineered UiO-66-NH_2 (A-aUiO) with missing linkers to act as active centers for CO_2 reduction. In photocatalytic systems using water as proton sources and isopropanol as sacrificial agents, the resultant Ir_1/A-aUiO particle photocatalyst showed desirable photocatalytic performance in CO_2 reduction to HCOOH with a yield of 0.51 mmol g^{-1} h^{-1} and an apparent quantum efficiency (AQE) of 2.51%, as well as good recyclability at 420 nm on the gas–liquid–solid reaction interface. Such promising performance stemmed from the strong interactions between the oxide clusters of the defect-engineered MOF matrix and Ir SAs, which could finely control the electronic structure of Ir species, resulting in Ir SAs becoming more positively charged (+3 to +4) compared with Ir clusters and NPs. The positively charged Ir SAs were responsible for the activation of CO_2, which could effectively trap the photogenerated electrons provided by the A-aUiO matrix and subsequently lead to photocatalytic CO_2 reduction. Moreover, under similar conditions, the authors found that the apparent activation energy for HCOOH generation of Ir_1/A-aUiO (9.8 kJ mol^{-1}) was much lower than that of IrNPs/A-aUiO and Ir_x/A-aUiO based on the results of the Arrhenius plots (Fig. 9h). Thus, the photocatalytic performance of Ir_1/A-aUiO was far higher than that of other samples toward HCOOH generation. In contrast, it was understandable that Ir NPs on A-aUiO possessed a much lower activity and selectivity (16.5%). In order to have a close picture of the reaction route for CO_2 photoreduction, the authors employed FTIR to investigate the intermediate product of this reaction. Generally, the peaks attributed to the surface carbonic acid species at 1497 and 1433 cm^{-1} could be found on A-aUiO and Ir_1/A-aUiO in the dark, indicating that the hydroxyls from the Zr oxo of A-aUiO adsorbed the CO_2 molecules. As shown in Fig. 9i, some new infrared peaks of HCOO* species could be found on Ir_1/A-aUiO which were not observed on A-aUiO upon irradiation, suggesting HCOOH as the final product of this reaction. In addition, based on the thermodynamics, since the CB (−0.60 V *vs.* NHE) of A-aUiO was more negative compared to the CO_2 reduction potential of CO_2/HCOOH (−0.37 V *vs.* NHE) (Fig. 9j), the photocatalytic CO_2 reduction route for HCOOH generation could proceed smoothly. Specifically, the Ir_1 active species with protons (from water) and photogenerated electrons (from A-aUiO excited by a 300W Xe lamp) hydrogenated adsorbed CO_2 on A-aUiO to produce HCOOH. More importantly, the high porosity of Ir_1/A-aUiO membranes could facilitate high-throughput reaction interfaces of CO_2 to the active centers compared to conventional gas–liquid–solid reaction interfaces (Fig. 9k), which could significantly improve the availability of CO_2 around active Ir species and prevent competitive adsorption of liquid water. Subsequently, Ir_1/A-aUiO membranes exhibited a yield of 3.38 mmol g^{-1} h^{-1} with near-unity selectivity in the conversion of CO_2 to HCOOH, and high stability through the long-term (100 h) operation, which was 6.5 times higher than that of Ir_1/A-aUiO particles.

Based on the above-mentioned examples of MOF-supported SACs for photocatalytic CO_2 processes, it is obvious that the decoration of SAs on MOFs could be a fascinating strategy for achieving efficient photocatalytic performance. The functional synergy between the SACs and the highly porous MOF can give MOF-supported SACs better photoactivity and selectivity than NPs/MOF at very low metal contents. Importantly, the strong bonding and suitable coordination environment provided by MOFs for SAs could allow them to carry out photocatalytic processes stably and efficiently. However, the research is still in its incipient stage and there is still a need to develop MOF-supported SACs for efficient photocatalytic CO_2 reduction through rational design. In addition, considering the current ambiguity regarding the actual photocatalytic CO_2 reduction pathways on MOF-based supported SACs, future efforts to investigate such reactions through available and highly accurate characterization tools are eagerly awaited.

5.2. Hydrogen generation

Hydrogen is considered to be an environmentally friendly and sustainable energy source and is emerging as a great alternative to fossil fuels in the future.[136,137] Therefore, it is important to develop an economical, simple and green technology for

hydrogen generation.[138,139] Solar-driven water decomposition with high flexibility and applicability is regarded as a green and promising technology for generation of renewable and clean hydrogen.[140] Since the pioneering exploration by Fujishima *et al.*, various types of photocatalysts have been widely developed to generate hydrogen from water under light irradiation.[141] At present, noble metal-based materials are the most effective photocatalysts for hydrogen generation, but their low reserve and high cost seriously restrict their large-scale application.[142] Accordingly, there is an urgent need to explore efficient photocatalysts with low or non-noble metal content. Fortunately, MOF-supported SACs can address these challenges to a large degree. For example, porphyrin struts as organic linkers in MOFs with well-defined square-planar trapping sites can robustly and uniformly capture SAs to achieve high performance. Fang *et al.* fabricated atomically dispersed Pt SAs inside a highly stable Al-based porphyrinic MOF (Al-TCPP) by a hydrothermal reaction, and the existence of monodispersed Pt atoms was unambiguously demonstrated by XAFS and HAADF-STEM analysis (Fig. 8b, e and f).[68] FT-EXAFS spectra demonstrated the absence of Pt–Cl and Pt–Pt bonds and but the presence of monodispersed Pt–N sites in Al-TCPP0.1Pt with Pt loadings of 0.07 wt%. The authors further employed ultrafast TA spectroscopy to track the charge carrier kinetics in these samples in real time, and the biexponential fitting results indicated that Al-TCPP0.1Pt showed a dramatical acceleration of the TA kinetics compared to Al–TCPP–PtNPs (Fig. 10a). Apparently, downsizing Pt NPs into SAs and then stabilizing by the enormous pyrrolic structures on the surface of Al-TCPP allowed for a stronger interaction between Al-TCPP and Pt SAs, which therefore opened a highly efficient electron transfer channel. It could facilitate the transfer of photogenerated charge carriers from the bulk to the Al-TCPP0.1Pt surface for taking part in the photocatalytic reaction, which was undoubtedly beneficial to the improvement of photocatalytic performance. As a consequence, in CH_3CN solutions with triethanolamine as the sacrificial agent, the resultant Al-TCPP0.1Pt with maximum atomic utilization demonstrated superb photocatalytic performance towards hydrogen generation with a yield of 129 μmol g^{-1} h^{-1}, which was much higher than that of Pt NPs/Al-TCPP (Fig. 10b). DFT calculations unveiled that the introduction of atomically dispersed Pt atoms on the surface of Al-TCPP led to an appealing hydrogen binding energy (ΔG_{H^*} = 0.05 eV), thereby contributing to the significantly accelerated activity of hydrogen generation. Importantly, the recovery of Al-TCPP0.1Pt showed that no noticeable performance decline took place in hydrogen generation over four photocatalytic runs, demonstrating the excellent reusability of photocatalysts (Fig. 10c).

In the pursuit of better substance delivery and more accessible active sites, He *et al.* employed a facile solvothermal strategy to stabilize various noble-metal SAs in highly stable Zr-based porphyrinic MOF hollow nanotubes (HNTMs) (Fig. 5c).[59] In sharp contrast to the bulk MOFs, hollow MOFs with pyrrolic N_4 sites featured a high surface area, easy mass diffusion and low density, allowing them to better stabilize SAs. Various single noble-metal atoms have been successfully stabilized by the well-defined coordination sites of porphyrin units in HNTMs as confirmed by HAADF-STEM observations and XAFS results. Remarkably, by virtue of the unique hollow structure, light-harvesting ability and synergistic interaction between Ir and Pt, HNTM-Ir/Pt exhibited the highest photocatalytic hydrogen generation performance (201.9 mmol g^{-1} h^{-1}) under visible-light irradiation, exceeding the performance of HNTM-Pt and HNTM-Ir by 3.6 and 27 times, respectively. In particular, the synergistic interaction between Ir and Pt was responsible for the enhanced activity, *i.e.*, the porphyrin–Ir units served as photosensitizers for strong light-harvesting capability, while the porphyrin–Pt units behaved as active sites to complete hydrogen generation. Specifically, the porphyrin organic linkers could be photoexcited under visible-light irradiation to generate electron–hole pairs, and then electrons were efficiently transferred to active sites to participate in hydrogen generation. Besides, HNTM-Ir/Pt also showed excellent recyclability with no noticeable decrease in activity after three consecutive cycles. In another work, Zuo *et al.* first developed a new surfactant-stabilized coordination approach to stabilize Pt SAs with an ultrahigh loading (12.0 wt%) using ultrathin (2.4 ± 0.9 nm) 2D porphyrinic Cu-based MOF nanosheets (PtSA-MNSs) as hosts (Fig. 6c).[77] Owing to their high Pt loading content, in aqueous solution with ascorbic acid as a sacrificial agent, PtSA-MNSs demonstrated highly efficient photocatalytic hydrogen generation performance with a rate of 11 320 μmol g^{-1} h^{-1} for the reported MOF-based photocatalysts under visible-light irradiation. The accelerated hydrogen generation performance could be attributed to the synergistic action of Pt SAs and Cu nodes in the MOF nanosheets. Specifically, the formation of ultrathin 2D MOF morphology with abundant available sites through the Cu nodes was conducive to the photogenerated electron transfer among the connected photosensitive porphyrin rings, while the ultrahigh concentration of Pt SAs effectively trapped the photogenerated electrons and served as active sites for hydrogen generation. Moreover, cycling experiments suggested that the PtSA-MNS photocatalyst also featured remarkable stability with 7% decay in the hydrogen generation rate after four reaction cycles. Strikingly, PtSA-MNSs could also retain their highly efficient photocatalytic activity after being drop-cast onto solid substrates, revealing their great promise for practical solar-driven hydrogen generation.

Multifunctional and structure-tailorable MOFs have abundant coordination sites to anchor metal SAs due to their abundant inorganic metal nodes and organic linkers. Apart from the square-planar coordination sites of porphyrins, amine groups ($-NH_2$) with lone-pair electrons in organic linkers can also effectively anchor single transition metal atoms through strong coordination. Yan *et al.* employed a facile pyrolysis process to firmly anchor two kinds of Ru species (Ru-NPs/SAs and Ru-SAs) firmly supported on MIL-125-NH_2 derived N-doped TiO_2/C (N-TC) for photocatalytic hydrogen generation (Fig. 7a).[116] During the synthesis process, the injection of Ru^{3+} ions determined not only the dispersion state and final size of Ru species, but also the morphology structure of N-TC. They found that the doping of N and the introduction of atomically dispersed Ru species

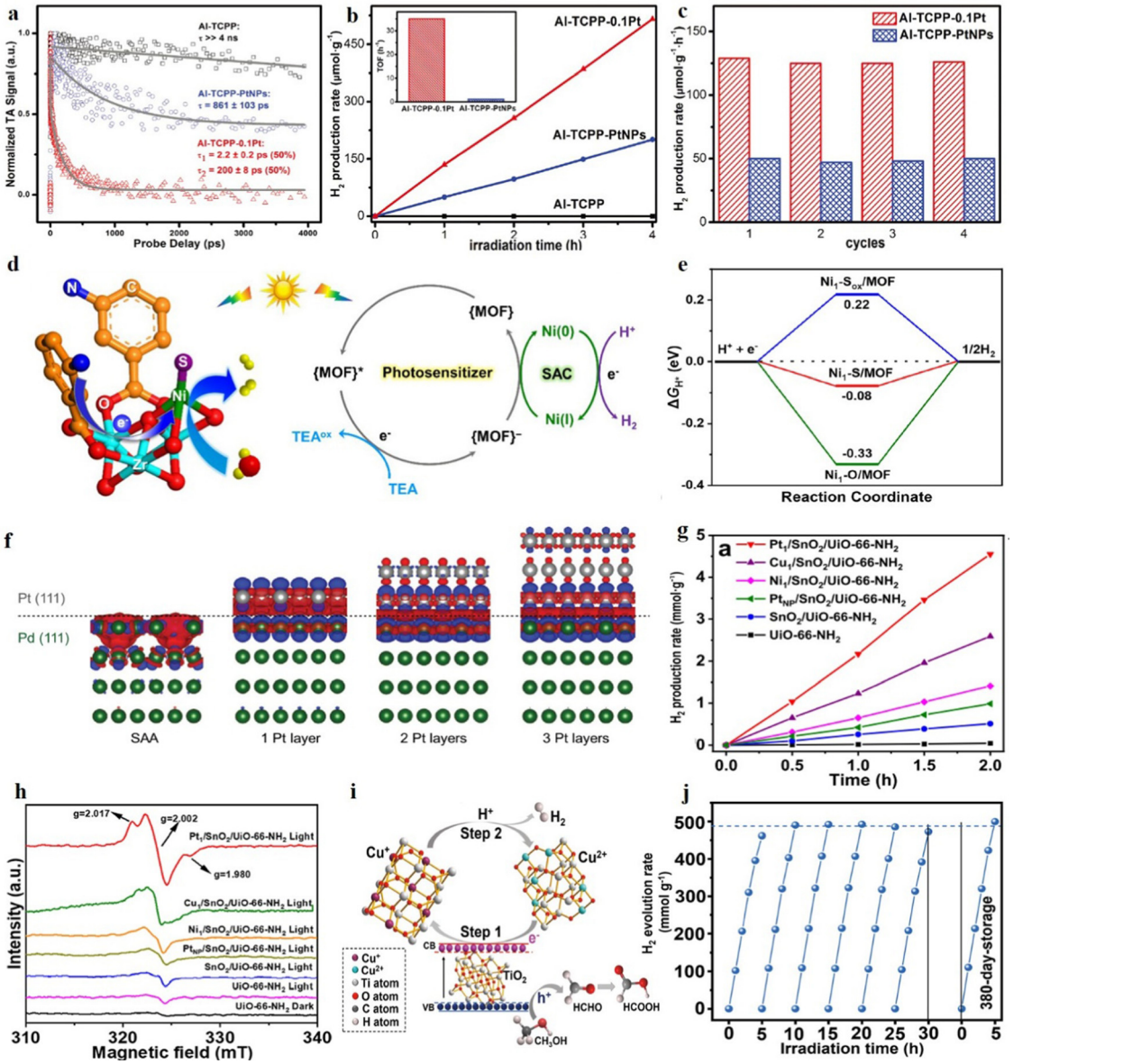

Fig. 10 (a) The ultrafast TA kinetics for Al–TCPP–0.1Pt, Al–TCPP–PtNPs and Al-TCPP. (b) Photocatalytic hydrogen generation rates of Al–TCPP–0.1Pt, Al–TCPP–PtNPs and Al-TCPP. (c) Three cycles of photocatalytic hydrogen generation experiments using Al–TCPP–0.1Pt, Al–TCPP–PtNPs and Al–TCPP–0.1Pt. Reproduced with permission from ref. 68. Copyright 2018, Wiley-VCH. (d) Schematic illustration of the proposed mechanism for photocatalytic hydrogen generation over Ni_1–S/MOF. (e) Calculated free energy diagram for photocatalytic hydrogen generation over Ni_1–S/MOF. Reproduced with permission from ref. 70. Copyright 2021, American Chemical Society. (f) Schematic illustration of the charge redistribution and charge density difference over Pd@Pt NPs with SAA and different Pt layer thickness. Blue represents a decrease in electron density, while red indicates an increase in electron density. Reproduced with permission from ref. 143. Copyright 2020, Oxford Academic. (g) Photocatalytic hydrogen generation rates of $Pt_1/SnO_2/UiO\text{-}66\text{-}NH_2$ and other samples. (h) EPR spectra of $Pt_1/SnO_2/UiO\text{-}66\text{-}NH_2$ and other samples. Reproduced with permission from ref. 78. Copyright 2021, Wiley-VCH. (i) Schematic illustration of the photocatalytic hydrogen generation mechanism on CuSA–TiO_2. (j) The photocatalytic performance of CuSA–TiO_2 during six cyclic experiments and after storing in the lab for 380 days. Reproduced with permission from ref. 60. Copyright 2022, Nature Publishing Group.

contributed to the generation of more Ti^{3+}–O_v defects, which could favor more trapping sites to facilitate the separation and transfer of charge carriers. Note that the photocatalytic activity (58.3 μmol h^{-1}) of Ru-SAs@NTC was significantly enhanced due to the inherently high functional and advanced atomic configurations after the introduction of atomically dispersed Ru species. Astonishingly, Ru-NPs/SAs@NTC exhibited better photocatalytic activity than Ru-SAs@NTC with a rate of 100 μmol h^{-1}, although Ru-SAs@NTC featured the greatest charge separation efficiency. The authors ascribed the superior hydrogen generation activity of Ru-NPs/SAs@NTC to the synergistic coupling effect of Ru SAs and Ru NPs rather than the charge separation efficiency. Firstly, Ru NPs could manipulate the electronic structure of atomically dispersed Ru species to ameliorate the water adsorption ability

to facilitate hydrogen generation. Secondly, Ru-NPs/SAs@NTC possessed a larger flat-band potential shift than Ru-SAs@N-TC, indicating that Ru-NPs/SAs@NTC had a smaller CB bending degree and therefore thermodynamically faster charge transfer. Moreover, the large specific surface area of Ru-NPs/SAs@N-TC ($307.5\ m^2\ g^{-1}$) also could facilitate mass transfer and enhance the photocatalytic performance.

Intriguingly, it is worth noting that the coordination microenvironment of SAs also deeply influences photocatalytic efficiency. Ma *et al.* found that the coordination microenvironment modulation of Ni_1 SAs could play a critical role in photocatalysis based on their synthesis of Ni_1–X/MOF (X = S, O, S_{ox} (ox = oxidation); MOF = UiO-66-NH_2) with various modulated microenvironments around the Ni_1 sites on Zr_6 oxo clusters *via* the post-synthetic modification strategy (Fig. 4a).[70] Atomic structural analysis unveiled that the five-coordinated Ni^{2+} sites were anchored onto –O/OH_x groups from the defects of Zr_6–oxo clusters, and all the single Ni_1 atoms in Ni_1–X/MOF were well maintained after modulation of the coordination environment by post-synthetic modification. The light-harvesting ability of MOFs was not apparently changed after modification with Ni_1–X. Among them, all Ni_1–X/MOF SACs with high-loading (>4 wt%), featuring high atomic availability and accessibility to the linkers, presented extraordinarily enhanced charge transfer, well in advance of the corresponding parent MOF and Ni NPs-decorated MOF. Remarkably, the Ni_1–S/MOF involving Ni^{2+}/MOF for sulfidation exhibited the best hydrogen generation efficiency among all the non-noble metal photocatalysts with a yield rate of 1360 μmol g^{-1} h^{-1}, which was much superior to all other counterparts in this work. The isolated Ni_1 sites in Ni_1–S/MOF possessed the stronger electron-donating microenvironment and closer proximity to the organic linker (as the photosensitizing unit) than the other counterparts such as Ni_1–S_{ox}/MOF and Ni_1–O/MOF, which could deeply extract the photogenerated electrons and effectively suppress radiative electron–hole recombination. Additionally, DFT calculations revealed that Ni_1–S/MOF SACs with the favorable coordination environment exhibited an optimized H adsorption ($\Delta G_{H^*} = -0.08$ eV), indicating a faster proton/electron transfer and thus facilitating hydrogen generation (Fig. 10d). Hence, Ni_1–S/MOF exhibited the best activity in photocatalysis. Upon irradiation, the amine-functionalized linker in UiO-66-NH_2 would absorb photons to generate electron–hole pairs, while the electrons were transferred to the Zr oxo cluster to form the reductive active center. Then, the electrons would be further transferred to the Ni_1–S site to form the unique Ni(I) center to facilitate hydrogen generation (Fig. 10e). More importantly, the cycling tests demonstrated that Ni_1–S/MOF was an extremely durable SAC with no decrease in activity after at least six cycles, indicating a strong bonding between atomically dispersed Ni atoms and the MOF support.

Alloying strategies of SAs to achieve single-atom alloys (SAAs) are a highly effective way to affect their photocatalytic performance due to their tailorable geometry chemistry and coordination environment, as well as synergistic interactions originating from bimetallic components. Pan *et al.* first precisely regulated the Pt coordination environment of Pd@Pt NPs stabilized by UiO-66-NH_2 from core–shell to SAA to form Pd_{10}@Pt_x/UiO-66-NH_2 (10 and x refer to the mass permeability of Pd and Pt to the MOF in wt% during synthesis, respectively) for hydrogen generation.[143] The authors found that the Pt shell thickness could be finely manipulated by altering the proportion of Pd/Pt precursors. When Pt content was reduced to Pd_{10}@Pt_1/UiO-66-NH_2, the atomically dispersed Pt atoms were successfully formed on the Pd surface, which was unambiguously confirmed by the atomic structural analysis. Given the different working functions of Pt and Pd, electrons tended to leave Pd (of lower work function and with electrons less tightly bound) and travel to Pt, and the evolution of the Pd@Pt NP structure from core–shell to SAA would cause charge redistribution (charge density change between Pt and Pd) and affect the surface charge state of Pt. DFT calculations confirmed this and revealed the enhanced charge accumulation on the Pt surface along with the decrease in the number of Pt layers (Fig. 10f). As expected, Pd_{10}@Pt_1/UiO-66-NH_2 with a SAA structure possessed the highest number of Pt–Pd coordination sites, the strongest charge redistribution effect and the richest electrons surrounding Pt. Moreover, the photoelectrochemical measurements had also validated the superiority of the SAA structure in enhancing the charge transfer efficiency of the prepared samples. Under visible-light irradiation, UiO-66-NH_2 could be excited to produce photogenerated electron–hole pairs, which would be transferred to Pd and then to Pt due to the Schottky junction, and finally involved in hydrogen generation. Accordingly, Pd_{10}@Pt_1/UiO-66-NH_2 exhibited prominent hydrogen generation performance, with a generation rate of 1200.5 μmol g^{-1} h^{-1}, which exceeded the performance of all the investigated samples. Notably, Pd_{10}@Pt_1/UiO-66-NH_2 delivered remarkable long-term recyclability and stability, with negligible activity decay after five consecutive runs and 25 h operation. Unexpectedly, when the Pt content continued to decrease (x from 1 to 0.3), the photocatalytic hydrogen generation performance slightly declined, and the authors attributed this to the decreased Pt sites in the photocatalyst.

Specific structures and components are generally required when using metal oxo clusters or organic linkers in MOFs as coordination sites to anchor SAs, restricting their synthetic ubiquity. To address this point, Sui *et al.* developed a universal synthetic strategy to anchor SAs on MOFs.[78] Notably, by the virtue of SnO_2 with high stability and strong interaction as a mediator or adaptor, it was not only possible to anchor different single metal sites such as Pt, Ni, Cu, *etc.*, but also to vary the MOF support (UiO-66-NH_2, PCN-222 and DUT-67) to achieve M_1/SnO_2/MOF. The presence of high-density Pt SAs was reflected by HAADF-STEM images, where atomically dispersed Pt atoms were clearly identified as bright spots. Furthermore, the authors thought that each Pt atom was coordinated by about four oxygen atoms with no presence of Pt–Cl bonds or Pt–Pt bonds (Fig. 8g and h). Importantly, with the pre-introduction of Sn^{2+} in the synthetic process, the immobilization of various atomically dispersed metal species (Pt, Ni, Cu, *etc.*) onto diverse MOFs (UiO-66-NH_2, PCN-222 and DUT-67) could be achieved.

The morphology and crystallinity of MOFs remained almost constant after the modification. The UV-vis DRS spectra indicated that the intrinsic absorption of MOFs was not significantly affected by SA incorporation. Combining the photoluminescence, photocurrent and electrochemical impedance test, it was revealed that Pt_1/SnO_2/MOF featured the highest charge transfer efficiency. Accordingly, by the virtue of maximized atomic utilization of SAs, the photocatalytic hydrogen generation activity of Pt_1/SnO_2/MOF was approximately 5-fold higher than that of Pt NPs ($\sim$2.5 nm)/SnO_2/UiO-66-NH_2, and other SA (Cu and Ni) photocatalysts also exhibited much stronger hydrogen generation activity than that of their counterparts (Cu and Ni NPs) (Fig. 10g). Although Cu_1 and Ni_1 had the same chemical microenvironment and support as Pt, Pt_1/SnO_2/UiO-66-NH_2 exhibited a better hydrogen generation rate of 2167 μmol g^{-1} h^{-1}. The authors attributed the greatly improved photocatalytic activity to the fact that Pt SAs could behave as cocatalysts to trap electrons for accelerating the charge carrier migration and the low overpotential of Pt_1/SnO_2/UiO-66-NH_2 for fast hydrogen desorption. In detail, the amino functionalized organic linker in Pt_1/SnO_2/UiO-66-NH_2 would be photoexcited to generate electron–hole pairs, and the photogenerated electrons migrated to the Zr oxo clusters through a linker-to-cluster charge transfer process and further to the Pt SAs for subsequent hydrogen generation. The electron paramagnetic resonance (EPR) results (Fig. 10h) also directly indicated that Pt_1/SnO_2/UiO-66-NH_2 showed the strongest EPR signals and possessed greatly accelerated electron transfer, which was consistent with its stunning photocatalytic activity. Moreover, DFT calculations further validated that Pt_1/SnO_2/UiO-66-NH_2 possessed the most suitable hydrogen binding free energy (ΔG_{H^*} to −0.28 eV) to guarantee the fastest hydrogen desorption.

Moreover, Zhang *et al.* reported the large loading and highly dispersed Cu SAs anchored on MIL-125 derived TiO_2, and the composite exhibited promising photocatalytic activity.[60] Generally, Cu^{2+} species were first loaded onto MIL-125 to generate metal oxygen–titanium bonds and then calcined to yield CuSA–TiO_2, where Cu SAs were firmly and strongly anchored on TiO_2. The formation of the Cu SAs anchored on MIL-125 derived TiO_2 was evidenced by employing the HAADF-STEM characterization, revealing that Cu SAs were solely bound in the Ti vacancies *via* the Cu–O–Ti structure and no other Cu species (*e.g.*, clusters or nanoparticles) were observed (Fig. 8c and d). The dissociated Cu^{2+} in MIL-125 was more readily coordinated to oxygen and the very large surface area of MIL-125 as an intermediate (1361 m^2 g^{-1}) maximized the exposed sites for Cu SAs anchored on TiO_2. After calcination, the strongly anchored and highly dispersed Cu SAs on TiO_2 effectively trapped the photogenerated electrons, resulting in dramatically enhanced interfacial charge separation in CuSA–TiO_2, followed by the electron reduction of water to release hydrogen. Theoretical calculations of carrier transfer had also validated that this enhanced interfacial charge separation efficiency on the prepared CuSA–TiO_2 was because Cu–O as the electron bridge guided more efficient photogenerated charge carrier vertical flow from Cu active sites for hydrogen generation. As a result, under a Xe lamp using methanol as a hole scavenger, the best-in-class CuSA–TiO_2 photocatalyst with a relatively high loading content of about 1.5 wt% demonstrated an ultrahigh hydrogen generation rate of 101.7 mmol g^{-1} h^{-1} with an apparent quantum efficiency of 56% at 365 nm, outperforming other reported photocatalysts. The authors also performed isotopic tracing experiments to track the source of protons, and the results indicated that the hydrogen source was primarily from water and partially from methanol. Moreover, it was found that the strongly bonded Cu SAs on TiO_2 induced a self-healing and continuous photocatalytic process (Fig. 10i). Specifically, Cu^{2+} species were reduced to Cu^+ by photogenerated electrons causing the faster electron transfer, and then Cu^+ would return to Cu^{2+} by reducing water to release hydrogen. More importantly, the six consecutive experiments and long-term chronoamperometric tests have shown that CuSA–TiO_2 had excellent long-term stability and reproducibility, which was of great importance for industrial applications (Fig. 10j).

According to the recent progress, it can be concluded that MOF-supported SACs have demonstrated fascinating activity for hydrogen generation, due to the accelerated charge carrier separation and enormous photocatalytically active sites. Although considerable efforts and progress have been made, there is still a long way to go for the widespread use of MOF-based supported SACs in hydrogen generation. The successful laboratory synthesis often requires overcoming a number of factors before it can be scaled up to large-scale synthesis. Besides, photocatalytic hydrogen generation cannot be performed without sacrificial agents such as TEOA, methanol and so on, which remains economically and ecologically problematic. Hence, designing SACs with high performance, excellent stability, low cost and synthetic universality should be considered a priority in future research.

6. Concluding remarks and perspectives

The rational design of state-of-the-art photocatalysts with high activity and low cost is of prime importance for the conversion of the incident solar energy into renewable and sustainable energy. In consequence, single atom photocatalysts have gradually developed into a new frontier in photocatalytic research. The unique atomic structures, well-defined active sites and unsaturated coordination environments of SAs make them attractive in terms of boosting the efficiency of energy conversion systems compared with the conventional metal nanoparticle or nanocluster photocatalysts. Particularly, for the synthesis of stable and high-metal-loading SAs, MOFs have recently emerged as ideal platforms to support SAs for versatile applications in photocatalysis. Specifically, MOF supports for SAs present a variety of advantages over conventional supports: (1) the metal clusters and organic linkers in MOFs could offer abundant potential coordination sites to anchor SAs with strong affinity; (2) the high permanent porosity and surface area of MOFs could greatly enhance the interactions with the reactant molecules and facilitate mass transfer; (3) the coordination microenvironment of SAs could be easily modulated to

dramatically improve reaction activity and/or selectivity; (4) well-defined SAs supported on MOFs could provide the possibility of a thorough understanding of structure–performance relationships; and (5) the long-term stability and high loading of SAs supported on semiconductor-like MOFs would offer the possibility of a great leap from laboratory to practical applications for single atom photocatalysts in photocatalytic research.

Despite the tremendous progress in MOF-supported SACs for photocatalysis, the exploration of MOF-based supported SACs is still in its infancy. Substantial challenges and future perspectives should be significantly considered and addressed to achieve high-performance MOF-supported SACs and propel the practicality of SACs in photocatalysis.

(1) Although initial success has been achieved in recent years in the preparation of high loading SAs (>4 wt%) using MOFs as supports compared with conventional supports, the synthesis of single atom photocatalysts with higher-metal-loading still remains a challenging problem. There is no doubt that increasing the metal loading to a reasonable level can further boost photocatalytic performance. However, the content of SAs in MOFs tends to reach a certain level where the high surface energy of the SAs leads to their aggregation. Also, the above discussion has demonstrated that the SAs can be strongly stabilized by MOFs, but some MOF-supported SACs still exhibit insufficient durability with reduced activity and destabilization of SAs during photocatalytic cycles, limiting their widespread use in practical applications.[77,93] Therefore, a better understanding of the formation process and mechanism of MOF-supported SACs is desired to optimize the synthesis conditions for firmly stabilizing SAs and increasing their contents. Moreover, SAs supported on MOF are generally coordinated with the adjacent atoms in the organic linkers or anchored to the chelate sites on the metal clusters. These often require specific MOF components and structures to introduce SAs, greatly limiting the generality of the synthetic approach. Up to now, among the thousands of MOFs reported, only a pitifully small number of MOFs (UiO-66-NH_2, PCN-222, MIL-101-NH_2(Al), MIL-125-NH_2(Al) and so on) have been chosen as precursors/supports to stabilize SACs. For this reason, it is important to explore and develop innovative and alternative general strategies for the controlled synthesis of MOF-supported SAC photocatalysts with high metal content.

(2) More powerful characterization techniques should be developed. There is still a significant gap in the fundamental understanding of the practical role of the synergistic mechanism between SAs and MOFs in improving photocatalytic performance. Clearly, well-defined MOF anchored SAs can serve as a promising model to construct coordination configurations of SAs supported on MOFs for investigating the electronic structures and coordination environment of SAs at the atomic level. However, current tools for characterizing SAs have difficulty in distinguishing small differences in coordination structures around the metal SAs. More powerful characterization techniques that can precisely identify the coordination configuration of SAs supported on MOFs are in high demand. Moreover, during the photocatalytic reaction, the characterization should not only monitor the formation of SAs, but also examine the real chemical state changes of the MOF-supported SAC photocatalysts before and after the reaction, thus revealing the real synergistic mechanism between SAs and MOFs and the corresponding dynamic evolution process. This can contribute to an in-depth insight into the photocatalytic reaction mechanism and the rational design of efficient photocatalysts.

(3) Theoretical calculations have become a powerful tool to study the local atom–support interactions, coordination environments and electronic structures of MOF-based SACs as well as the charge transfer during the photocatalytic process, which robustly reveal the working mechanism of SACs in boosting photocatalytic reactions. However, theoretical modelling of the dynamics of SAs in photocatalytic reactions limits the reasonable knowledge of the roles of SAs in photocatalytic performance. This may require the development of innovative simulation methods and the combination of different simulation methods (such as molecular dynamics and time-resolved DFT) to model dynamic changes of the SAs, not only during the photocatalytic process but also during their formation process, which could unravel the real effect of the SAs and the corresponding dynamic evolution process. Moreover, detailed experimental evidence and theoretical work should be combined to comprehensively understand the metal–MOF support interactions and the corresponding complete photocatalytic mechanism in real scenarios. Overall, the accurate structure models of SAs that reflect the activity of SACs, clear pictures of the dynamic evolution of SAs (active sites), and experimental data reflecting the intermediates during the photocatalytic process are sufficient requirements for an in-depth and clear understanding of the photocatalytic mechanism. Additionally, the rational design, discovery and the corresponding exploration of applications for MOF-supported SAC photocatalysts are still in their nascent stages. Therefore, it is highly desirable to develop active machine learning combined with high-throughput calculations to predict the coordination structure of SAs in MOF-supported SACs, the photocatalytic activity of MOF-supported SACs and the corresponding applicable targeted reaction conditions. This may not only facilitate the rational development of highly efficient MOF-supported SACs, but also greatly reduce the cost of selecting suitable MOF-supported SACs.

(4) To further increase the intrinsic photocatalytic activity, both highly reactive SAs and MOF supports should be particularly considered. For highly reactive SAs, the intrinsic photocatalytic activity could be designed by modulating the coordination of SAs, which can be achieved by tuning the electronic structure and geometry of the SAs to modify the binding energy between reactants and SAs and optimize the reaction pathway during the surface reaction. The strategy of tuning the coordination microenvironment can be achieved by first designing SACs with unsaturated coordination structures supported on MOFs, followed by post-synthetic modifications with diverse functional groups. For MOF supports, bulk MOF-supported SACs restrict to some extent the accessibility of substrate transfer and available open active sites. However, the structural tailorability and high porosity of MOF supports can be readily and conveniently adapted to hollow or ultrathin 2D

structures of MOFs to anchor SAs with high accessibility, respectively, thus accelerating mass transportation and reserving highly available open sites.

(5) Exploring the synergistic interactions that exist between various types of SAs on the same MOF support holds considerable potential for controlling the overall photocatalytic performance and deepening the knowledge of the multiphase photocatalytic mechanism. Due to their particular structural advantages, MOF supports have the ability to support various types of SAs. Hence, the controllable synthesis of more than one kind of SA supported on the same MOF support should be taken into account. The synergistic effects among these SAs will be able to offer multifunctional active sites to greatly modify the reaction paths for the reactant, thus significantly accelerating the reaction process and obviously enhancing the photocatalytic performance.

(6) Systematically regulating the charge state of surface-active SAs would not only contribute to an in-depth understanding of the photoactivation path of MOF-supported SACs, but also provide guidance for the rational design of effective photocatalysts. The SA alloying strategy has been demonstrated to be a highly effective way of influencing their photocatalytic performance.[143] The geometric/strain and synergistic effects between these bimetallic components may cause a change in the charge density around the SAs. In other words, the electronic structure, charge density and geometry chemistry of SAs could be accurately tailored through changing the structure of bimetallic NPs from core–shell to SAA, thereby greatly enhancing photocatalysis. Hence, changing the structure of bimetallic NPs from core–shell to SAA may offer a reasonable and deployable approach for developing the rational design of efficient photocatalysts.

(7) The application of MOF-supported SACs should be widened to various photocatalysis-related fields. In addition to the above-mentioned applications involving photocatalysis such as hydrogen generation and CO_2 reduction, there are many other emerging applications for energy conversion and environmental remediation such as photocatalytic N_2 fixation, photocatalytic degradation of organic pollutants and so on, which are rarely exploited through MOF-supported SACs. Moreover, MOF-supported SAC photocatalysts have focused on idealized experimental conditions, and rarely have been able to take into account the influence of real environmental factors on their photocatalytic performance. Considering the huge potential of SACs and the diversity of options for MOF supports, if MOF-supported SAC photocatalysts with desirable properties can be designed and built, they will be the game-changing tools to achieve high activity, adaptability, versatility as well as selectivity in photocatalysis.

Conflicts of interest

The authors declare no conflict of interest.

Acknowledgements

This study was financially supported by the Program for the National Natural Science Foundation of China (51909084, 51909085, 51979103), China Postdoctoral Science Foundation Funded Project (2018M642977), the Natural Science Foundation of Hunan Province, China (2020JJ5055, 2020JJ5069), and the Fundamental Research Funds for the Central Universities (531118010247).

References

1 M. S. Dresselhaus and I. L. Thomas, *Nature*, 2001, **414**, 332–337.
2 N. S. Lewis and D. G. Nocera, *Proc. Natl. Acad. Sci. U. S. A.*, 2006, **103**, 15729–15735.
3 A. Listorti, J. Durrant and J. Barber, *Nat. Mater.*, 2009, **8**, 929–930.
4 Y. Tachibana, L. Vayssieres and J. R. Durrant, *Nat. Photonics*, 2012, **6**, 511–518.
5 D. Kim, K. K. Sakimoto, D. Hong and P. Yang, *Angew. Chem., Int. Ed.*, 2015, **54**, 3259–3266.
6 S. Sultan, J. N. Tiwari, A. N. Singh, S. Zhumagali, M. Ha, C. W. Myung, P. Thangavel and K. S. Kim, *Adv. Energy Mater.*, 2019, **9**, 1900624.
7 Y. Chen, S. Ji, W. Sun, Y. Lei, Q. Wang, A. Li, W. Chen, G. Zhou, Z. Zhang, Y. Wang, L. Zheng, Q. Zhang, L. Gu, X. Han, D. Wang and Y. Li, *Angew. Chem., Int. Ed.*, 2020, **59**, 1295–1301.
8 P. Dong, Y. Wang, A. Zhang, T. Cheng, X. Xi and J. Zhang, *ACS Catal.*, 2021, **11**, 13266–13279.
9 C. Gao, S. Chen, Y. Wang, J. Wang, X. Zheng, J. Zhu, L. Song, W. Zhang and Y. Xiong, *Adv. Mater.*, 2018, **30**, 1704624.
10 B.-H. Lee, E. Gong, M. Kim, S. Park, H. R. Kim, J. Lee, E. Jung, C. W. Lee, J. Bok, Y. Jung, Y. S. Kim, K.-S. Lee, S.-P. Cho, J.-W. Jung, C.-H. Cho, S. Lebegue, K. T. Nam, H. Kim, S.-I. In and T. Hyeon, *Energy Environ. Sci.*, 2022, **15**, 601–609.
11 Y. Li, B. Li, D. Zhang, L. Cheng and Q. Xiang, *ACS Nano*, 2020, **14**, 10552–10561.
12 A. Wang, J. Li and T. Zhang, *Nat. Rev. Chem.*, 2018, **2**, 65–81.
13 X.-F. Yang, A. Wang, B. Qiao, J. Li, J. Liu and T. Zhang, *Acc. Chem. Res.*, 2013, **46**, 1740–1748.
14 B. Qiao, A. Wang, X. Yang, L. F. Allard, Z. Jiang, Y. Cui, J. Liu, J. Li and T. Zhang, *Nat. Chem.*, 2011, **3**, 634–641.
15 X. Li, W. Bi, L. Zhang, S. Tao, W. Chu, Q. Zhang, Y. Luo, C. Wu and Y. Xie, *Adv. Mater.*, 2016, **28**, 2427–2431.
16 C. Gao, J. Low, R. Long, T. Kong, J. Zhu and Y. Xiong, *Chem. Rev.*, 2020, **120**, 12175–12216.
17 K. Jiang, M. Luo, Z. Liu, M. Peng, D. Chen, Y.-R. Lu, T.-S. Chan, F. M. F. de Groot and Y. Tan, *Nat. Commun.*, 2021, **12**, 1687.
18 S. Yang, J. Kim, Y. J. Tak, A. Soon and H. Lee, *Angew. Chem., Int. Ed.*, 2016, **55**, 2058–2062.
19 Z. Wang, E. Almatrafi, H. Wang, H. Qin, W. Wang, L. Du, S. Chen, G. Zeng and P. Xu, *Angew. Chem., Int. Ed.*, 2022, e202202338.

20 Z. Zeng, Y. Su, X. Quan, W. Choi, G. Zhang, N. Liu, B. Kim, S. Chen, H. Yu and S. Zhang, *Nano Energy*, 2020, **69**, 104409.
21 P. Zhou, F. Lv, N. Li, Y. Zhang, Z. Mu, Y. Tang, J. Lai, Y. Chao, M. Luo, F. Lin, J. Zhou, D. Su and S. Guo, *Nano Energy*, 2019, **56**, 127–137.
22 T. E. James, S. L. Hemmingson and C. T. Campbell, *ACS Catal.*, 2015, **5**, 5673–5678.
23 A. Corma, P. Concepción, M. Boronat, M. J. Sabater, J. Navas, M. J. Yacaman, E. Larios, A. Posadas, M. A. López-Quintela, D. Buceta, E. Mendoza, G. Guilera and A. Mayoral, *Nat. Chem.*, 2013, **5**, 775–781.
24 Y. Wang, J. Mao, X. Meng, L. Yu, D. Deng and X. Bao, *Chem. Rev.*, 2019, **119**, 1806–1854.
25 B. Zhang, T. Fan, N. Xie, G. Nie and H. Zhang, *Adv. Sci.*, 2019, **6**, 1901787.
26 Y. He, S. Liu, C. Priest, Q. Shi and G. Wu, *Chem. Soc. Rev.*, 2020, **49**, 3484–3524.
27 Y. Zhu, J. Sokolowski, X. Song, Y. He, Y. Mei and G. Wu, *Adv. Energy Mater.*, 2020, **10**, 1902844.
28 J. Yang, W. Li, D. Wang and Y. Li, *Adv. Mater.*, 2020, **32**, 2003300.
29 X. Cui, W. Li, P. Ryabchuk, K. Junge and M. Beller, *Nat. Catal.*, 2018, **1**, 385–397.
30 B. Han, Y. Guo, Y. Huang, W. Xi, J. Xu, J. Luo, H. Qi, Y. Ren, X. Liu, B. Qiao and T. Zhang, *Angew. Chem., Int. Ed.*, 2020, **59**, 11824–11829.
31 R. Lang, X. Du, Y. Huang, X. Jiang, Q. Zhang, Y. Guo, K. Liu, B. Qiao, A. Wang and T. Zhang, *Chem. Rev.*, 2020, **120**, 11986–12043.
32 J. Lin, A. Wang, B. Qiao, X. Liu, X. Yang, X. Wang, J. Liang, J. Li, J. Liu and T. Zhang, *J. Am. Chem. Soc.*, 2013, **135**, 15314–15317.
33 Q. Wang, X. Huang, Z. L. Zhao, M. Wang, B. Xiang, J. Li, Z. Feng, H. Xu and M. Gu, *J. Am. Chem. Soc.*, 2020, **142**, 7425–7433.
34 K. Jiang, S. Siahrostami, T. Zheng, Y. Hu, S. Hwang, E. Stavitski, Y. Peng, J. Dynes, M. Gangisetty, D. Su, K. Attenkofer and H. Wang, *Energy Environ. Sci.*, 2018, **11**, 893–903.
35 J. Yang, B. Chen, X. Liu, W. Liu, Z. Li, J. Dong, W. Chen, W. Yan, T. Yao, X. Duan, Y. Wu and Y. Li, *Angew. Chem., Int. Ed.*, 2018, **57**, 9495–9500.
36 S. Sun, G. Zhang, N. Gauquelin, N. Chen, J. Zhou, S. Yang, W. Chen, X. Meng, D. Geng, M. N. Banis, R. Li, S. Ye, S. Knights, G. A. Botton, T.-K. Sham and X. Sun, *Sci. Rep.*, 2013, **3**, 1775.
37 S. Wei, A. Li, J.-C. Liu, Z. Li, W. Chen, Y. Gong, Q. Zhang, W.-C. Cheong, Y. Wang, L. Zheng, H. Xiao, C. Chen, D. Wang, Q. Peng, L. Gu, X. Han, J. Li and Y. Li, *Nat. Nanotechnol.*, 2018, **13**, 856–861.
38 H. Zhang, S. Hwang, M. Wang, Z. Feng, S. Karakalos, L. Luo, Z. Qiao, X. Xie, C. Wang, D. Su, Y. Shao and G. Wu, *J. Am. Chem. Soc.*, 2017, **139**, 14143–14149.
39 L. Jiao, R. Zhang, G. Wan, W. Yang, X. Wan, H. Zhou, J. Shui, S.-H. Yu and H.-L. Jiang, *Nat. Commun.*, 2020, **11**, 2831.
40 X. Wen, Q. Zhang and J. Guan, *Coord. Chem. Rev.*, 2020, **409**, 213214.
41 Z. Wang, Z. Zeng, H. Wang, G. Zeng, P. Xu, R. Xiao, D. Huang, S. Chen, Y. He, C. Zhou, M. Cheng and H. Qin, *Coord. Chem. Rev.*, 2021, **439**, 213902.
42 H. Liu, M. Cheng, Y. Liu, G. Zhang, L. Li, L. Du, B. Li, S. Xiao, G. Wang and X. Yang, *Coord. Chem. Rev.*, 2022, **458**, 214428.
43 Q. Yang, Q. Xu and H.-L. Jiang, *Chem. Soc. Rev.*, 2017, **46**, 4774–4808.
44 N. Cheng, L. Zhang, K. Doyle-Davis and X. Sun, *Electrochem. Energy Rev.*, 2019, **2**, 539–573.
45 Y.-N. Gong, L. Jiao, Y. Qian, C.-Y. Pan, L. Zheng, X. Cai, B. Liu, S.-H. Yu and H.-L. Jiang, *Angew. Chem., Int. Ed.*, 2020, **59**, 2705–2709.
46 T. He, S. Chen, B. Ni, Y. Gong, Z. Wu, L. Song, L. Gu, W. Hu and X. Wang, *Angew. Chem., Int. Ed.*, 2018, **57**, 3493–3498.
47 A. J. Howarth, Y. Liu, P. Li, Z. Li, T. C. Wang, J. T. Hupp and O. K. Farha, *Nat. Rev. Mater.*, 2016, **1**, 15018.
48 Z. Liang, C. Qu, D. Xia, R. Zou and Q. Xu, *Angew. Chem., Int. Ed.*, 2018, **57**, 9604–9633.
49 D.-D. Ma and Q.-L. Zhu, *Coord. Chem. Rev.*, 2020, **422**, 213483.
50 Y. J. Colon and R. Q. Snurr, *Chem. Soc. Rev.*, 2014, **43**, 5735–5749.
51 N. Stock and S. Biswas, *Chem. Rev.*, 2012, **112**, 933–969.
52 Y. Liu, H. Cheng, M. Cheng, Z. Liu, D. Huang, G. Zhang, B. Shao, Q. Liang, S. Luo, T. Wu and S. Xiao, *Chem. Eng. J.*, 2020, **417**, 127914.
53 G. Zhang, D. Huang, M. Cheng, L. Lei, S. Chen, R. Wang, W. Xue, Y. Liu, Y. Chen and Z. Li, *J. Mater. Chem. A*, 2020, **8**, 17883–17906.
54 X. Zheng, P. Li, S. Dou, W. Sun, H. Pan, D. Wang and Y. Li, *Energy Environ. Sci.*, 2021, **14**, 2809–2858.
55 Z.-H. Xue, D. Luan, H. Zhang and X. W. Lou, *Joule*, 2022, **6**, 92–133.
56 Z. Song, L. Zhang, K. Doyle-Davis, X. Fu, J.-L. Luo and X. Sun, *Adv. Energy Mater.*, 2020, **10**, 2001561.
57 A. Han, B. Wang, A. Kumar, Y. Qin, J. Jin, X. Wang, C. Yang, B. Dong, Y. Jia, J. Liu and X. Sun, *Small Methods*, 2019, **3**, 1800471.
58 L. Jiao and H.-L. Jiang, *Chem*, 2019, **5**, 786–804.
59 T. He, S. Chen, B. Ni, Y. Gong, Z. Wu, L. Song, L. Gu, W. Hu and X. Wang, *Angew. Chem., Int. Ed.*, 2018, **57**, 3493–3498.
60 Y. Zhang, J. Zhao, H. Wang, B. Xiao, W. Zhang, X. Zhao, T. Lv, M. Thangamuthu, J. Zhang, Y. Guo, J. Ma, L. Lin, J. Tang, R. Huang and Q. Liu, *Nat. Commun.*, 2022, **13**, 58.
61 G. Wang, C. T. He, R. Huang, J. Mao, D. Wang and Y. Li, *J. Am. Chem. Soc.*, 2020, **142**, 19339–19345.
62 P. Zhang, J. Zhang and J. Gong, *Chem. Soc. Rev.*, 2014, **43**, 4395–4422.
63 T. Simon, M. T. Carlson, J. K. Stolarczyk and J. Feldmann, *ACS Energy Lett.*, 2016, **1**, 1137–1142.
64 T. Gershon, B. Shin, N. Bojarczuk, M. Hopstaken, D. B. Mitzi and S. Guha, *Adv. Energy Mater.*, 2015, **5**, 1400849.

65 J. Di, C. Chen, S.-Z. Yang, S. Chen, M. Duan, J. Xiong, C. Zhu, R. Long, W. Hao, Z. Chi, H. Chen, Y.-X. Weng, J. Xia, L. Song, S. Li, H. Li and Z. Liu, *Nat. Commun.*, 2019, **10**, 2840.
66 Y. Zhang, B. Xia, J. Ran, K. Davey and S. Z. Qiao, *Adv. Energy Mater.*, 2020, **10**, 1903879.
67 Y. Xue, B. Huang, Y. Yi, Y. Guo, Z. Zuo, Y. Li, Z. Jia, H. Liu and Y. Li, *Nat. Commun.*, 2018, **9**, 1460.
68 X. Fang, Q. Shang, Y. Wang, L. Jiao, T. Yao, Y. Li, Q. Zhang, Y. Luo and H. L. Jiang, *Adv. Mater.*, 2018, **30**, 1705112.
69 A. M. Abdel-Mageed, B. Rungtaweevoranit, M. Parlinska-Wojtan, X. Pei, O. M. Yaghi and R. J. Behm, *J. Am. Chem. Soc.*, 2019, **141**, 5201–5210.
70 X. Ma, H. Liu, W. Yang, G. Mao, L. Zheng and H. L. Jiang, *J. Am. Chem. Soc.*, 2021, **143**, 12220–12229.
71 R. Lang, W. Xi, J.-C. Liu, Y.-T. Cui, T. Li, A. F. Lee, F. Chen, Y. Chen, L. Li, L. Li, J. Lin, S. Miao, X. Liu, A.-Q. Wang, X. Wang, J. Luo, B. Qiao, J. Li and T. Zhang, *Nat. Commun.*, 2019, **10**, 234.
72 Y. Xiong, W. Sun, P. Xin, W. Chen, X. Zheng, W. Yan, L. Zheng, J. Dong, J. Zhang, D. Wang and Y. Li, *Nat. Commun.*, 2020, **32**, e2000896.
73 B. Qiao, J. Liu, Y.-G. Wang, Q. Lin, X. Liu, A. Wang, J. Li, T. Zhang and J. Liu, *ACS Catal.*, 2015, **5**, 6249–6254.
74 J. Jones, H. Xiong, A. T. DeLaRiva, E. J. Peterson, P. Hien, S. R. Challa, G. Qi, S. Oh, M. H. Wiebenga, X. I. P. Hernandez, Y. Wang and A. K. Datye, *Science*, 2016, **353**, 150–154.
75 Y. Chen, S. Ji, C. Chen, Q. Peng, D. Wang and Y. Li, *Joule*, 2018, **2**, 1242–1264.
76 Z. Li, D. Wang, Y. Wu and Y. Li, *Natl. Sci. Rev.*, 2018, **5**, 673–689.
77 Q. Zuo, T. Liu, C. Chen, Y. Ji, X. Gong, Y. Mai and Y. Zhou, *Angew. Chem., Int. Ed.*, 2019, **58**, 10198–10203.
78 J. Sui, H. Liu, S. Hu, K. Sun, G. Wan, H. Zhou, X. Zheng and H. L. Jiang, *Adv. Mater.*, 2021, **34**, 2109203.
79 S. K. Kaiser, E. Fako, G. Manzocchi, F. Krumeich, R. Hauert, A. H. Clark, O. V. Safonova, N. Lopez and J. Perez-Ramirez, *Nat. Catal.*, 2020, **3**, 376–385.
80 S. Li, B. Chen, Y. Wang, M.-Y. Ye, P. A. van Aken, C. Cheng and A. Thomas, *Nat. Mater.*, 2021, **20**, 1240–1247.
81 H. Yan, H. Cheng, H. Yi, Y. Lin, T. Yao, C. Wang, J. Li, S. Wei and J. Lu, *J. Am. Chem. Soc.*, 2015, **137**, 10484–10487.
82 J. H. Cavka, S. Jakobsen, U. Olsbye, N. Guillou, C. Lamberti, S. Bordiga and K. P. Lillerud, *J. Am. Chem. Soc.*, 2008, **130**, 13850–13851.
83 G. Férey, C. Mellot-Draznieks, C. Serre, F. Millange, J. Dutour, S. Surblé and I. Margiolaki, *Science*, 2005, **309**, 2040–2042.
84 P. Horcajada, S. Surblé, C. Serre, D.-Y. Hong, Y.-K. Seo, J.-S. Chang, J.-M. Grenèche, I. Margiolaki and G. Férey, *Chem. Commun.*, 2007, 2820–2822.
85 S. Surblé, F. Millange, C. Serre, T. Düren, M. Latroche, S. Bourrelly, P. L. Llewellyn and G. Férey, *J. Am. Chem. Soc.*, 2006, **128**, 14889–14896.
86 A. Fateeva, P. A. Chater, C. P. Ireland, A. A. Tahir, Y. Z. Khimyak, P. V. Wiper, J. R. Darwent and M. J. Rosseinsky, *Angew. Chem., Int. Ed.*, 2012, **51**, 7440–7444.
87 S. Guo, Y. Zhao, C. Wang, H. Jiang and G. J. Cheng, *ACS Appl. Mater. Interfaces*, 2020, **12**, 26068–26075.
88 S. Shang, W. Xiong, C. Yang, B. Johannessen, R. Liu, H. Y. Hsu, Q. Gu, M. K. H. Leung and J. Shang, *ACS Nano*, 2021, **15**, 9670–9678.
89 Q. Wang and K. Domen, *Chem. Rev.*, 2020, **120**, 919–985.
90 J. Zhang, T. Bai, H. Huang, M.-H. Yu, X. Fan, Z. Chang and X.-H. Bu, *Adv. Mater.*, 2020, **32**, 2004747.
91 X. Li, W. Bi, L. Zhang, S. Tao, W. Chu, Q. Zhang, Y. Luo, C. Wu and Y. Xie, *Adv. Mater.*, 2016, **28**, 2427–2431.
92 Q. Sun, N. Wang, T. Zhang, R. Bai, A. Mayoral, P. Zhang, Q. Zhang, O. Terasaki and J. Yu, *Angew. Chem., Int. Ed.*, 2019, **58**, 18570–18576.
93 H. Huang, K. Shen, F. Chen and Y. Li, *ACS Catal.*, 2020, **10**, 6579–6586.
94 B. An, J. Zhang, K. Cheng, P. Ji, C. Wang and W. Lin, *J. Am. Chem. Soc.*, 2017, **139**, 3834–3840.
95 K.-i Otake, Y. Cui, C. T. Buru, Z. Li, J. T. Hupp and O. K. Farha, *J. Am. Chem. Soc.*, 2018, **140**, 8652–8656.
96 Y.-Z. Chen, R. Zhang, L. Jiao and H.-L. Jiang, *Coord. Chem. Rev.*, 2018, **362**, 1–23.
97 X. Wang, W. Chen, L. Zhang, T. Yao, W. Liu, Y. Lin, H. Ju, J. Dong, L. Zheng, W. Yan, X. Zheng, Z. Li, X. Wang, J. Yang, D. He, Y. Wang, Z. Deng, Y. Wu and Y. Li, *J. Am. Chem. Soc.*, 2017, **139**, 9419–9422.
98 J. He, N. Li, Z.-G. Li, M. Zhong, Z.-X. Fu, M. Liu, J.-C. Yin, Z. Shen, W. Li, J. Zhang, Z. Chang and X.-H. Bu, *Adv. Funct. Mater.*, 2021, **31**, 2103597.
99 P. Ji, Y. Song, T. Drake, S. S. Veroneau, Z. Lin, X. Pan and W. Lin, *J. Am. Chem. Soc.*, 2018, **140**, 433–440.
100 Y.-S. Wei, M. Zhang, R. Zou and Q. Xu, *Chem. Rev.*, 2020, **120**, 12089–12174.
101 Y. C. Hao, L. W. Chen, J. Li, Y. Guo, X. Su, M. Shu, Q. Zhang, W. Y. Gao, S. Li, Z. L. Yu, L. Gu, X. Feng, A. X. Yin, R. Si, Y. W. Zhang, B. Wang and C. H. Yan, *Nat. Commun.*, 2021, **12**, 2682.
102 H. Imahori and S. Fukuzumi, *Adv. Mater.*, 2001, **13**, 1197–1199.
103 Z. Zhang, Y. Zhu, X. Chen, H. Zhang and J. Wang, *Adv. Mater.*, 2019, **31**, 1806626.
104 J. A. Johnson, J. Luo, X. Zhang, Y.-S. Chen, M. D. Morton, E. Echeverría, F. E. Torres and J. Zhang, *ACS Catal.*, 2015, **5**, 5283–5291.
105 P. Cai, M. Xu, S.-S. Meng, Z. Lin, T. Yan, H. F. Drake, P. Zhang, J. Pang, Z.-Y. Gu and H.-C. Zhou, *Angew. Chem., Int. Ed.*, 2021, **60**, 27258–27263.
106 A. G. Nugmanova, E. A. Safonova, A. E. Baranchikov, A. R. Tameev, A. V. Shkolin, A. A. Mitrofanov, A. A. Eliseev, I. N. Meshkov and M. A. Kalinina, *Appl. Surf. Sci.*, 2022, **579**, 152080.
107 L.-Y. Wu, Y.-F. Mu, X.-X. Guo, W. Zhang, Z.-M. Zhang, M. Zhang and T.-B. Lu, *Angew. Chem., Int. Ed.*, 2019, **58**, 9491–9495.
108 H. Zhang, J. Wei, J. Dong, G. Liu, L. Shi, P. An, G. Zhao, J. Kong, X. Wang, X. Meng, J. Zhang and J. Ye, *Angew. Chem., Int. Ed.*, 2016, **55**, 14310–14314.

109 J. Li, H. Huang, P. Liu, X. Song, D. Mei, Y. Tang, X. Wang and C. Zhong, *J. Catal.*, 2019, **375**, 351–360.
110 B. Liu, H. Shioyama, T. Akita and Q. Xu, *J. Am. Chem. Soc.*, 2008, **130**, 5390–5391.
111 S. Dang, Q.-L. Zhu and Q. Xu, *Nat. Rev. Mater.*, 2017, **3**, 17075.
112 Y.-S. Wei, M. Zhang, M. Kitta, Z. Liu, S. Horike and Q. Xu, *J. Am. Chem. Soc.*, 2019, **141**, 7906–7916.
113 Y. Chen, S. Ji, Y. Wang, J. Dong, W. Chen, Z. Li, R. Shen, L. Zheng, Z. Zhuang, D. Wang and Y. Li, *Angew. Chem., Int. Ed.*, 2017, **56**, 6937–6941.
114 R. Jiang, L. Li, T. Sheng, G. Hu, Y. Chen and L. Wang, *J. Am. Chem. Soc.*, 2018, **140**, 11594–11598.
115 Y. Qu, Z. Li, W. Chen, Y. Lin, T. Yuan, Z. Yang, C. Zhao, J. Wang, C. Zhao, X. Wang, F. Zhou, Z. Zhuang, Y. Wu and Y. Li, *Nat. Catal.*, 2018, **1**, 781–786.
116 B. Yan, D. Liu, X. Feng, M. Shao and Y. Zhang, *Adv. Funct. Mater.*, 2020, **30**, 2003007.
117 L. Jiao, G. Wan, R. Zhang, H. Zhou, S. H. Yu and H. L. Jiang, *Angew. Chem., Int. Ed.*, 2018, **57**, 8525–8529.
118 X. Xie, L. Peng, H. Yang, G. I. N. Waterhouse, L. Shang and T. Zhang, *Adv. Mater.*, 2021, **33**, e2101038.
119 P. Yin, T. Yao, Y. Wu, L. Zheng, Y. Lin, W. Liu, H. Ju, J. Zhu, X. Hong, Z. Deng, G. Zhou, S. Wei and Y. Li, *Angew. Chem., Int. Ed.*, 2016, **55**, 10800–10805.
120 C. Zhao, X. Dai, T. Yao, W. Chen, X. Wang, J. Wang, J. Yang, S. Wei, Y. Wu and Y. Li, *J. Am. Chem. Soc.*, 2017, **139**, 8078–8081.
121 J. Wang, Z. Huang, W. Liu, C. Chang, H. Tang, Z. Li, W. Chen, C. Jia, T. Yao, S. Wei, Y. Wu and Y. Li, *J. Am. Chem. Soc.*, 2017, **139**, 17281–17284.
122 J. Li, M. Chen, D. A. Cullen, S. Hwang, M. Wang, B. Li, K. Liu, S. Karakalos, M. Lucero, H. Zhang, C. Lei, H. Xu, G. E. Sterbinsky, Z. Feng, D. Su, K. L. More, G. Wang, Z. Wang and G. Wu, *Nat. Catal.*, 2018, **1**, 935–945.
123 X. Han, X. Ling, Y. Wang, T. Ma, C. Zhong, W. Hu and Y. Deng, *Angew. Chem., Int. Ed.*, 2019, **58**, 5359–5364.
124 X. X. Wang, D. A. Cullen, Y.-T. Pan, S. Hwang, M. Wang, Z. Feng, J. Wang, M. H. Engelhard, H. Zhang, Y. He, Y. Shao, D. Su, K. L. More, J. S. Spendelow and G. Wu, *Adv. Mater.*, 2018, **30**, 1706758.
125 X. Sun, A. I. Olivos-Suarez, D. Osadchii, M. J. V. Romero, F. Kapteijn and J. Gascon, *J. Catal.*, 2018, **357**, 20–28.
126 W. Chen, J. Pei, C.-T. He, J. Wan, H. Ren, Y. Wang, J. Dong, K. Wu, W.-C. Cheong, J. Mao, X. Zheng, W. Yan, Z. Zhuang, C. Chen, Q. Peng, D. Wang and Y. Li, *Adv. Mater.*, 2018, **30**, 1800396.
127 Z. Geng, Y. Liu, X. Kong, P. Li, K. Li, Z. Liu, J. Du, M. Shu, R. Si and J. Zeng, *Adv. Mater.*, 2018, **30**, 1803498.
128 E. Luo, H. Zhang, X. Wang, L. Gao, L. Gong, T. Zhao, Z. Jin, J. Ge, Z. Jiang, C. Liu and W. Xing, *Angew. Chem., Int. Ed.*, 2019, **58**, 12469–12475.
129 R. Lang, T. Li, D. Matsumura, S. Miao, Y. Ren, Y.-T. Cui, Y. Tan, B. Qiao, L. Li, A. Wang, X. Wang and T. Zhang, *Angew. Chem., Int. Ed.*, 2016, **55**, 16054–16058.
130 K. Ding, A. Gulec, A. M. Johnson, N. M. Schweitzer, G. D. Stucky, L. D. Marks and P. C. Stair, *Science*, 2015, **350**, 189–192.
131 Y. Liu, C. Tang, M. Cheng, M. Chen, S. Chen, L. Lei, Y. Chen, H. Yi, Y. Fu and L. Li, *ACS Catal.*, 2021, **11**, 13374–13396.
132 Y. Liu, D. L. Huang, M. Cheng, Z. F. Liu, C. Lai, C. Zhang, C. Y. Zhou, W. P. Xiong, L. Qin, B. B. Shao and Q. H. Liang, *Chem. Soc. Rev.*, 2020, **409**, 213220.
133 S. Cestellos-Blanco, H. Zhang, J. M. Kim, Y.-X. Shen and P. Yang, *Nat. Catal.*, 2020, **3**, 245–255.
134 A. Liu, W. Guan, Q. Cao, X. Ren, L. Gao, Q. Zhao and T. Ma, *New J. Chem.*, 2020, **44**, 8971–8976.
135 M. Elcheikh Mahmoud, H. Audi, A. Assoud, T. H. Ghaddar and M. Hmadeh, *J. Am. Chem. Soc.*, 2019, **141**, 7115–7121.
136 Z. Wang, C. Li and K. Domen, *Chem. Soc. Rev.*, 2019, **48**, 2109–2125.
137 S. Chen, T. Takata and K. Domen, *Nat. Rev. Mater.*, 2017, **2**, 17050.
138 P. Zhang and X. W. Lou, *Adv. Mater.*, 2019, **31**, 1804883.
139 G. Zhang, G. Liu, L. Wang and J. T. S. Irvine, *Chem. Soc. Rev.*, 2016, **45**, 5951–5984.
140 T. Hisatomi and K. Domen, *Nat. Catal.*, 2019, **2**, 387–399.
141 A. Fujishima and K. Honda, *Nature*, 1972, **238**, 37–38.
142 Y.-C. Zhang, N. Afzal, L. Pan, X. Zhang and J.-J. Zou, *Adv. Sci.*, 2019, **6**, 1900053.
143 Y. Pan, Y. Qian, X. Zheng, S.-Q. Chu, Y. Yang, C. Ding, X. Wang, S.-H. Yu and H.-L. Jiang, *Natl. Sci. Rev.*, 2020, **8**, nwaa224.

